



This is a repository copy of *Evaluation of spectral, optoelectrical, dielectric, magnetic, and morphological properties of RE<sup>3+</sup> (La<sup>3+</sup>, and Ce<sup>3+</sup>) and Co<sup>2+</sup> co-doped Zn<sub>0.75</sub> Cu<sub>0.25</sub> Fe<sub>2</sub> O<sub>4</sub> ferrites.*

White Rose Research Online URL for this paper:

<https://eprints.whiterose.ac.uk/178991/>

Version: Accepted Version

---

**Article:**

Rehman, A.U., Amin, N., Tahir, M.B. et al. (6 more authors) (2022) Evaluation of spectral, optoelectrical, dielectric, magnetic, and morphological properties of RE<sup>3+</sup> (La<sup>3+</sup>, and Ce<sup>3+</sup>) and Co<sup>2+</sup> co-doped Zn<sub>0.75</sub> Cu<sub>0.25</sub> Fe<sub>2</sub> O<sub>4</sub> ferrites. *Materials Chemistry and Physics*, 275. 125301. ISSN 0254-0584

<https://doi.org/10.1016/j.matchemphys.2021.125301>

---

© 2021 Elsevier B.V. This is an author produced version of a paper subsequently published in *Materials Chemistry and Physics*. Uploaded in accordance with the publisher's self-archiving policy. Article available under the terms of the CC-BY-NC-ND licence (<https://creativecommons.org/licenses/by-nc-nd/4.0/>).

**Reuse**

This article is distributed under the terms of the Creative Commons Attribution-NonCommercial-NoDerivs (CC BY-NC-ND) licence. This licence only allows you to download this work and share it with others as long as you credit the authors, but you can't change the article in any way or use it commercially. More information and the full terms of the licence here: <https://creativecommons.org/licenses/>

**Takedown**

If you consider content in White Rose Research Online to be in breach of UK law, please notify us by emailing [eprints@whiterose.ac.uk](mailto:eprints@whiterose.ac.uk) including the URL of the record and the reason for the withdrawal request.



[eprints@whiterose.ac.uk](mailto:eprints@whiterose.ac.uk)  
<https://eprints.whiterose.ac.uk/>

# Evaluation of spectral, optoelectrical, dielectric, magnetic, and morphological properties of RE<sup>3+</sup> (La<sup>3+</sup>, and Ce<sup>3+</sup>) and Co<sup>2+</sup> co-doped Zn<sub>0.75</sub>Cu<sub>0.25</sub>Fe<sub>2</sub>O<sub>4</sub> ferrites

Atta Ur Rehman<sup>a</sup>, Nasir Amin<sup>a</sup>, Muhammad Bilal Tahir<sup>b</sup>, Muhammad Ajaz un Nabi<sup>a</sup>, N. A. Morley<sup>c</sup>, Meshal Alzaid<sup>d</sup>, Mongi Amami<sup>e</sup>, Muhammad Imran Arshad<sup>a\*</sup>

<sup>a</sup>Department of Physics, Government College University, Faisalabad 38000, Pakistan.

<sup>b</sup>Department of Physics, Khwaja Fareed University of Engineering and information technology Rahim yar Khan 64200, Pakistan.

<sup>c</sup> Department of Materials Science and Engineering, The University of Sheffield, UK, S1 3JD.

<sup>d</sup>Physics Department, College of Science, Jouf University, Al-Jouf, Sakaka P.O. Box 2014, Saudi Arabia.

<sup>e</sup>Department of Chemistry College of Sciences, King khalid university, P.O. Box 9004, Abha, Saudi Arabia

\*Corresponding Author: [miarshadgcuf@gmail.com](mailto:miarshadgcuf@gmail.com)

## Abstract

Present work reports the synthesis of RE<sup>3+</sup> (La<sup>3+</sup>, and Ce<sup>3+</sup>) and Co<sup>2+</sup> co-doped Zn<sub>0.75</sub>Cu<sub>0.25</sub>Fe<sub>2</sub>O<sub>4</sub> samples powder using sol-gel auto combustion process. Rietveld refinement established the spinel matrix with the space group ( $Fd\bar{3}m$ ) and suggests that the uniform distribution of cations at the tetrahedral and octahedral lattice sites. The comparative study of crystallite size ( $D$ ) was found using the Scherrer's relation, Scherrer's plot, Williamson-Hall (W-H), and Size-Strain (SS) plot methods for the as-prepared ferrites. The absorption band analysis confirmed the characteristic band absorptions lie in the frequency range of  $(577.82 - 418.84) \times 10^2 \times \text{m}^{-1}$ . Moreover, the electrical resistivity ( $\rho$ ) measurements showed that the Co-Ce doped ZCF sample is highly resistive as compared to the other samples. The dielectric measurements revealed a dispersion pattern at lower frequencies and an almost frequency-independent pattern at higher frequencies. The field dependence of the  $dM/dH$  curve shows a magnetically well stable state and good crystallization cubic matrix of all the samples.

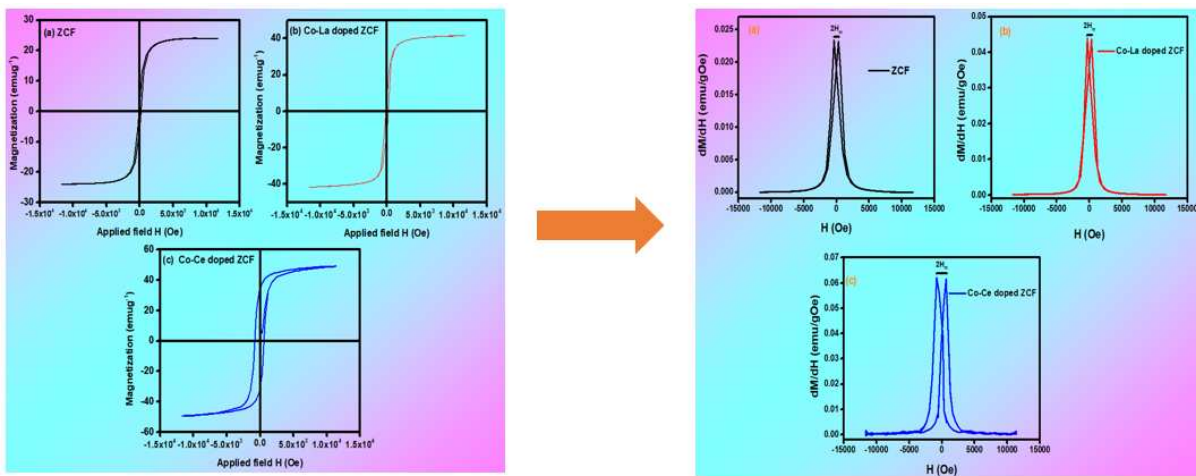
**Keywords:** sol-gel auto combustion; Rietveld refinement; absorption band; field dependence; dielectric; crystallization.

## Highlights

- Sol-gel auto-igniting process used to prepare  $\text{RE}^{3+}$  ( $\text{La}^{3+}$ , and  $\text{Ce}^{3+}$ ) and  $\text{Co}^{2+}$  co-doped  $\text{Zn}_{0.75}\text{Cu}_{0.25}\text{Fe}_2\text{O}_4$  samples powder.
- Rietveld refinement confirmed the uniform distribution of cations.
- The microwaves operating frequency ( $\omega_m$ ) lies within the range of 5.31 – 10.91 GHz.
- Well, crystallization and magnetic stability of all the as-prepared samples.

## Graphical Abstract

The field dependence of the  $dM/dH$  curve at 303 K suggests that the increasing peaks separation and height for the as-prepared ferrites are owing to the existence of good magnetic stability and crystallization.



## 1 Introduction

Nano ferrite's structural, optical, vibrational, electrical, dielectric, and magnetic properties can be changed with the substitution of divalent and trivalent cations. They are used in many applications including the biomedical field [1], electronics technology [2], wastewater treatments [3], and energy storage devices [4]. The spinel structure nano ferrites are also used in microwave applications [5], in permanent magnet applications for simple DC motors [6], in antimicrobial applications [7], and even as a promising cathode material in Li-ion batteries [8]. The physical properties of the nano ferrites are highly affected by their chemical composition and their preparation technique [9]. Numerous preparation techniques have been established to prepare nano ferrites and their properties have been studied *via* different analytical techniques. For the synthesis of spinel matrix nano ferrites, the microemulsion process [10], the self-igniting auto combustion route [11, 12], the hydrothermal method [13], co-precipitation [14-17], and a lot more other techniques have been used. Sol-gel auto combustion route was observed to be better because of fine surface morphology, better homogeneity of particles, excellent properties, and low-temperature preparation [18]. Moreover, tuning the physical properties is possible through the substitution of appropriate divalent and trivalent cations at the lattice sites of nano ferrites. That is, partially doping of certain selected cations at the tetrahedral (*A*-) or octahedral (*B*-) sites or even at both sites will significantly change the properties of nanocrystalline ferrites. Such efforts have been reported previously and include Elayakumar *et al.* [19] reported a self-igniting method for the synthesis of Ce<sup>3+</sup> doped cobalt nano ferrites. They also stated that there was a decrease in crystallite size with an increase in Ce<sup>3+</sup> concentration, with the minimum value of 16.53 nm at  $x = 0.5$ . Bahar *et al.* studied the impact of La<sup>3+</sup> on numerous properties of Zn<sup>2+</sup> soft ferrites and described that the crystallite size obtained from XRD analysis decreased with La<sup>3+</sup> content increase [20]. Kumar *et al.* developed  $CoLa_xFe_{2-x}O_4$  nano ferrites using the co-precipitation technique. The impact of La<sup>3+</sup> cations on the electrical and dielectric parameters of Co<sup>2+</sup> ferrites was investigated. The dielectric loss decreased with La<sup>3+</sup> concentration, and at  $x = 0.2$  had a minimum value. The DC electrical resistivity of pure cobalt ferrites is  $6.465 \times 10^5 \Omega \text{ cm}$  and increased with the dopant content [21].

In the present work,  $Zn_{0.75}Cu_{0.25}Fe_2O_4$  (ZCF),  $Zn_{0.5}Co_{0.25}Cu_{0.25}La_{0.125}Fe_{1.875}O_4$  (Co-La doped ZCF), and  $Zn_{0.5}Co_{0.25}Cu_{0.25}Ce_{0.125}Fe_{1.875}O_4$  (Co-Ce doped ZCF) samples were prepared by the sol-gel auto-combustion route. Rietveld refinement analysis for cation distribution,

comparative study crystallite size, the optoelectrical, dielectric, magnetic, morphological, and chemical composition analysis were reported.

## 2. Experimental Part

### 2.1 Method of Preparation

To synthesize ZCF, Co-La doped ZCF, and Co-Ce doped ZCF sample powder, the sol-gel auto igniting process was used. For this purpose, highly pure nitrates including [La (NO<sub>3</sub>)<sub>3</sub>.6H<sub>2</sub>O], [Cu (NO<sub>3</sub>)<sub>2</sub>.6H<sub>2</sub>O], [Ce (NO<sub>3</sub>)<sub>3</sub>.6H<sub>2</sub>O], [Zn (NO<sub>3</sub>)<sub>2</sub>.6H<sub>2</sub>O], [Fe (NO<sub>3</sub>)<sub>3</sub>.9H<sub>2</sub>O], [Co (NO<sub>3</sub>)<sub>2</sub>.6H<sub>2</sub>O] and citric acid (C<sub>6</sub>H<sub>8</sub>O<sub>7</sub>) as the fuel were mixed with deionized water in a beaker. Citric acid is inexpensive and is a more effective complexing agent than other organic fuels in producing fine ferrite powder with a smaller particle size. A homogenous solution of nitrates and citric acid was obtained after 30 mins continuous stirring with a molar ratio of 1:2 and the pH of the solution was attained to 7 by adding ammonia dropwise. It was kept on a magnetic stirrer at 353 K and the solution changed into a gel by increasing the temperature of the hot plate up to 473 K. The auto-combustion was observed and the viscous gel was converted into a powder. Finally, the as-prepared powder was calcined at 1073 K for 8 h and then grounded to obtain a fine powder. The step-by-step process of synthesis is depicted in Fig. 1.

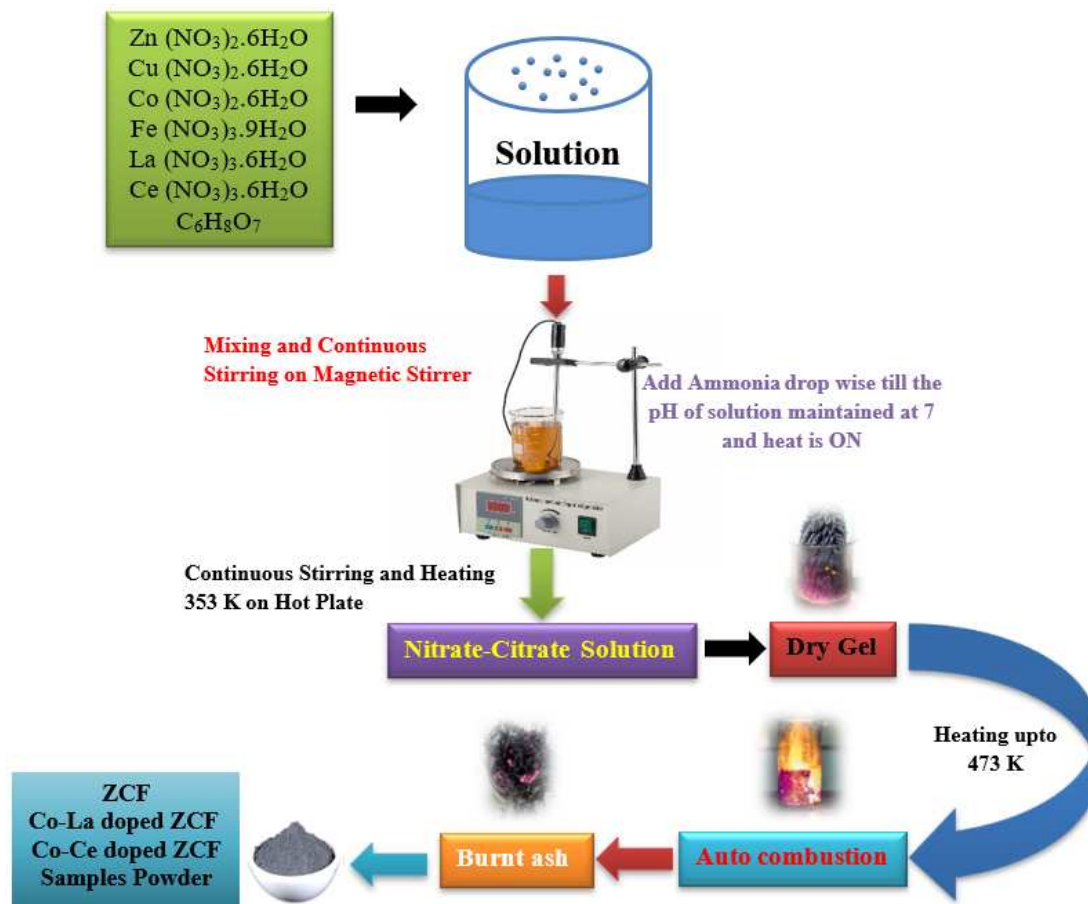


Fig. 1 The step-by-step process of preparation of ferrites powder

## 2.2 Characterization techniques

Bruker D8 Advanced X-ray diffractometer (XRD) with Copper  $K_{\alpha}$  source ( $\lambda = 1.54 \text{ \AA}$ ) used for structural analysis and phase confirmation. Fourier transforms infrared (FTIR) spectroscopy was used to study the absorption bands. Keithley Electrometer Model 2401 was used for current-voltage ( $I$ - $V$ ) measurements to determine electrical resistivity. The energy bandgap ( $E_g$ ) was determined through UV-visible spectroscopy. IM3533 series LCR Meter was used for dielectric measurements. Finally, a vibrating sample magnetometer (VSM) was used to study  $M$ - $H$  loops at 303 K. The Nova NanoSEM series 450 is used to examine the surface morphology and particle size from SEM images were found using ImageJ application software. Energy Dispersive X-Ray Analysis (EDX) was used to measure the chemical composition of the as-prepared samples.

## 3 Results and their discussions

### 3.1 XRD analysis

The XRD diffractograms of ZCF, Co-La doped ZCF, and Co-Ce doped ZCF samples were recorded within the range of  $20^{\circ} - 60^{\circ}$  as shown in Fig.2. The diffracted peaks are labeled with (220), (311), (222), (400), (422), and (511) planes, respectively. The planes confirmed the cubic  $FCC$  (face-centered cubic) crystal structure belongs to the space group ( $Fd-3m$ ) [9]. Excellent crystallinity was observed in all the samples, but additional peaks were also found in the Co-La doped ZCF sample [9, 22] and Co-Ce doped ZCF sample [23], which are denoted by (\*) and (#), respectively.

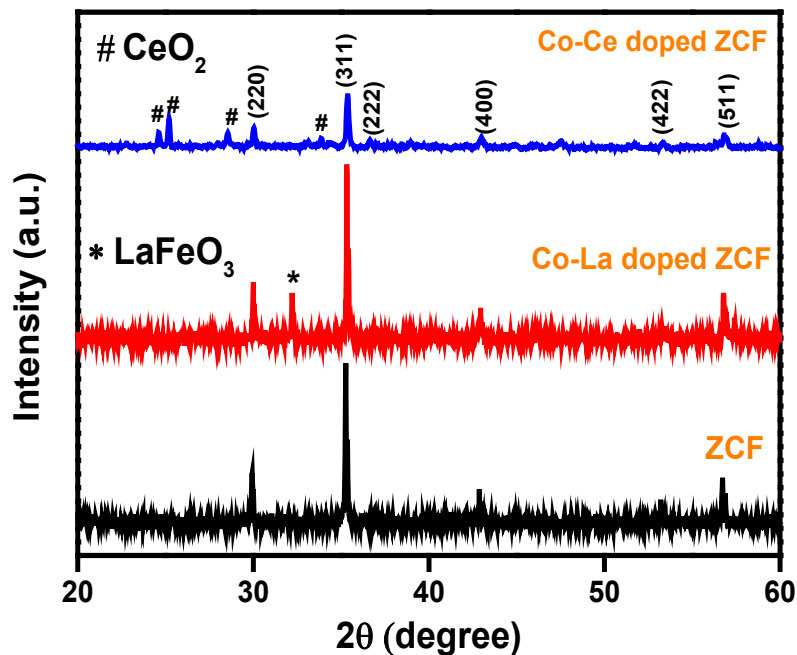


Fig. 2 XRD diffractograms for all the samples

### 3.1.1 Rietveld refinement

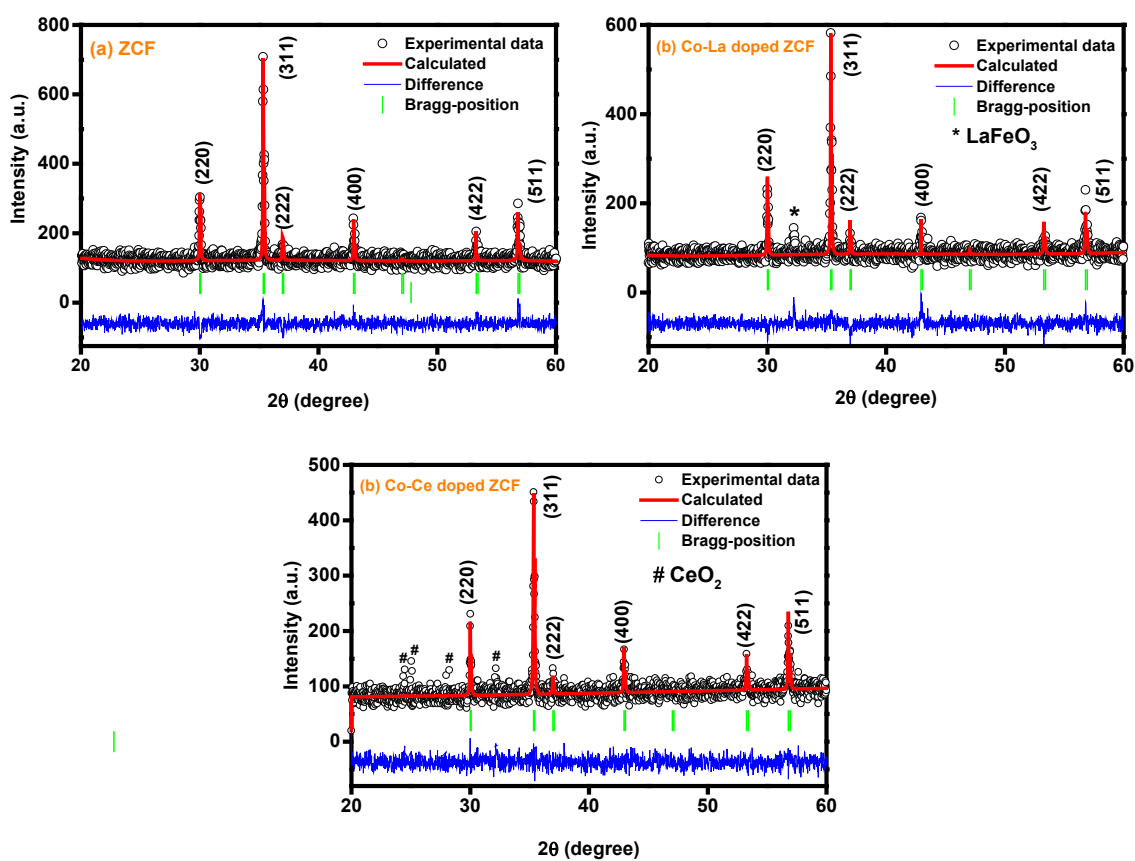
The Rietveld refinement XRD patterns at 303 K are shown in Fig. 3(a-c). The polycrystalline cubic spinel structure with a space group ( $Fd\bar{3}m$ ) is dominant in this figure, and it can be perfectly indexed to JCPDS#03-0864 [24]. Furthermore, the samples with the addition of  $\text{Co}^{2+}$  and rare earth ( $\text{La}^{3+}$  and  $\text{Ce}^{3+}$ ) cations, dual-phase nanostructures emerge, such as cubic spinel and orthorhombic  $\text{LaFeO}_3$  with space group ( $Pbnm$ ) for Co-La doped ZCF sample [9] and  $\text{CeO}_2$  for Co-Ce doped ZCF sample [25]. The existence of this phase is explained by the difference in ionic radii among  $\text{Zn}^{2+}$  (0.82 Å) [26],  $\text{Cu}^{2+}$  (0.70 Å) [27],  $\text{Co}^{2+}$  (0.82 Å) [26],  $\text{La}^{3+}$  (1.06 Å) [9],  $\text{Ce}^{3+}$  (1.02 Å) [25] and  $\text{Fe}^{3+}$  (0.67 Å) [9], with  $\text{Fe}^{3+}$  ions being replaced by  $\text{La}^{3+}$  and  $\text{Ce}^{3+}$  ions in Co-La doped ZCF and Co-Ce doped ZCF samples, respectively and reduced solubility in the Zn-Cu ferrites. After this point, rare earth ions start to accumulate around grain boundaries, forming a secondary phase [25].

The lattice constant ( $a$ ), unit cell volume ( $V$ ), site occupancy ( $g$ ), atomic position ( $x = y = z$ ), different reliability R-factors including weight R-profile ( $R_{wp}$ ) and R-expected ( $R_{exp}$ ), to check the structural reliability goodness-of-fit ( $\chi^2$ ) and cationic arrangements were obtained from Rietveld refinement and are given in Table 1 and Table 2. The lattice constant ( $a$ ) and volume of the unit cell ( $V$ ) was observed to decrease with the addition of dopant cations ( $\text{Co}^{2+}$ ,  $\text{La}^{3+}$ , and  $\text{Ce}^{3+}$ ) as compared to the pure ZCF sample (Table 1). The lattice parameters are shown to decrease with the dopants, due to the greater radii of  $\text{La}^{3+}$  (1.06 Å) and  $\text{Ce}^{3+}$  (1.02 Å) cations as compared to the  $\text{Fe}^{3+}$  (0.67 Å) cations. The value of reliability factors in Rietveld refinement was used to determine the quality of profile fit. The low R-factors indicate that the profile fit is of high quality [25].

The uniform cations distribution was observed from Rietveld refinement and is given in Table 2. There are 8 tetrahedral and 16 octahedral sites occupied by the di- and trivalent cations in the spinel structure. The  $\text{Zn}^{2+}$  cations occupy the tetrahedral site [28].  $\text{Co}^{2+}$  and  $\text{Fe}^{3+}$  occupy both tetrahedral and octahedral sites [29].  $\text{La}^{3+}$  replaces  $\text{Fe}^{3+}$  ions from the octahedral site [28] and  $\text{Ce}^{3+}$  also replaces trivalent  $\text{Fe}^{3+}$  cations at the octahedral site in the spinel matrix [16].

**Table 1** Rietveld refinements parameters of all the samples

Samples	ZCF	Co-La doped ZCF	Co-Ce doped ZCF
<b>Cell parameters</b>			
$a = b = c$ (Å)	8.4266	8.4111	8.4028
$\pm 0.005$			
$V$ (Å) <sup>3</sup>	598.35	595.05	593.31
<b>R-Factors</b>			
$R_{wp}$	11.9	8.87	1.34
$R_{exp}$	10.6	9.55	1.10
$\chi^2 = R_{wp}/R_{exp}$	11.2	9.53	1.17

**Fig. 3(a-c)** Rietveld refinements XRD patterns for all the samples

**Table 2** Atomic positions ( $x = y = z$ ), site occupancy ( $g$ ) and cationic distribution obtained from Rietveld refinement for as-prepared samples

Ions	ZCF		Co-La doped ZCF		Co-Ce doped ZCF	
	$x = y = z$	$g$	$x = y = z$	$g$	$x = y = z$	$g$
Zn <sup>2+</sup>	0.125	0.75	0.125	0.50	0.125	0.50
Cu <sup>2+</sup>	0.125	0.03	0.125	0.03	0.125	0.03
Co <sup>2+</sup>	0.125	0.00	0.125	0.03	0.125	0.03
Fe <sup>3+</sup>	0.125	0.22	0.125	0.44	0.125	0.44
Co <sup>2+</sup>	0.500	0.00	0.500	0.22	0.500	0.22
Cu <sup>2+</sup>	0.500	0.22	0.500	0.22	0.500	0.22
Fe <sup>3+</sup>	0.500	1.78	0.500	1.435	0.500	1.435
La <sup>3+</sup>	0.500	0.00	0.500	0.125	0.500	0.000
Ce <sup>3+</sup>	0.500	0.00	0.500	0.000	0.500	0.125
<b>Cationic distribution</b>	$(\text{Zn}_{0.75}^{2+}\text{Cu}_{0.03}^{2+}\text{Fe}_{0.22}^{3+})_{\text{A}}$ $[\text{Cu}_{0.22}^{2+}\text{Fe}_{1.78}^{3+}]_{\text{B}}$		$(\text{Zn}_{0.5}^{2+}\text{Co}_{0.03}^{2+}\text{Cu}_{0.03}^{2+}\text{Fe}_{0.44}^{3+})_{\text{A}}$ $[\text{Co}_{0.22}^{2+}\text{Cu}_{0.22}^{2+}\text{Fe}_{1.435}^{3+}\text{La}_{0.125}^{3+}]_{\text{B}}$		$(\text{Zn}_{0.5}^{2+}\text{Co}_{0.03}^{2+}\text{Cu}_{0.03}^{2+}\text{Fe}_{0.44}^{3+})_{\text{A}}$ $[\text{Co}_{0.22}^{2+}\text{Cu}_{0.22}^{2+}\text{Fe}_{1.435}^{3+}\text{Ce}_{0.125}^{3+}]_{\text{B}}$	

### 3.1.2 Comparative Crystalline Size Analysis

The average crystalline sizes ( $D$ ) were calculated using Scherrer's relation [16]. A decreasing trend in crystalline size is observed with the addition of the dopant cations when compared to the pure Zn-Cu nano ferrites (Table 3). Due to lattice strain and crystallite size peak broadening occurred and caused the crystal deformation. Also, have an inverse relation with crystallite size. X-ray peak broadening is divided into two parts instrumental and physical broadening. The instrumental and physical broadening of as-prepared powder was measured using FWHM (Full width at half maxima). The following relation is used to correct instrumental broadening [30]:

$$\beta = \beta_m^2 - \beta_i^2 \quad (1)$$

where  $\beta$ ,  $\beta_m$ ,  $\beta_i$  are corrected, measured, and instrumental broadening. By rearranging the Scherrer relation, we can write as:

$$\cos\theta = \frac{0.9\lambda}{D} \times \frac{1}{\beta} \quad (2)$$

The average crystallite size ( $D$ ) also finds out using the Scherrer plot ( $1/\beta$  vs  $\cos\theta$  plot) by taking the slope of linear fitting as shown in Fig.4(a-c), which is found as decreased from 76.15 nm to 55.66 nm with the substitution of dopant cations in the spinel matrix (Table 3). Scherrer relation only describes the impact of crystallite size on the peak broadening and does not explain the strain produced during crystal growth due to grain boundary and point defect [30].

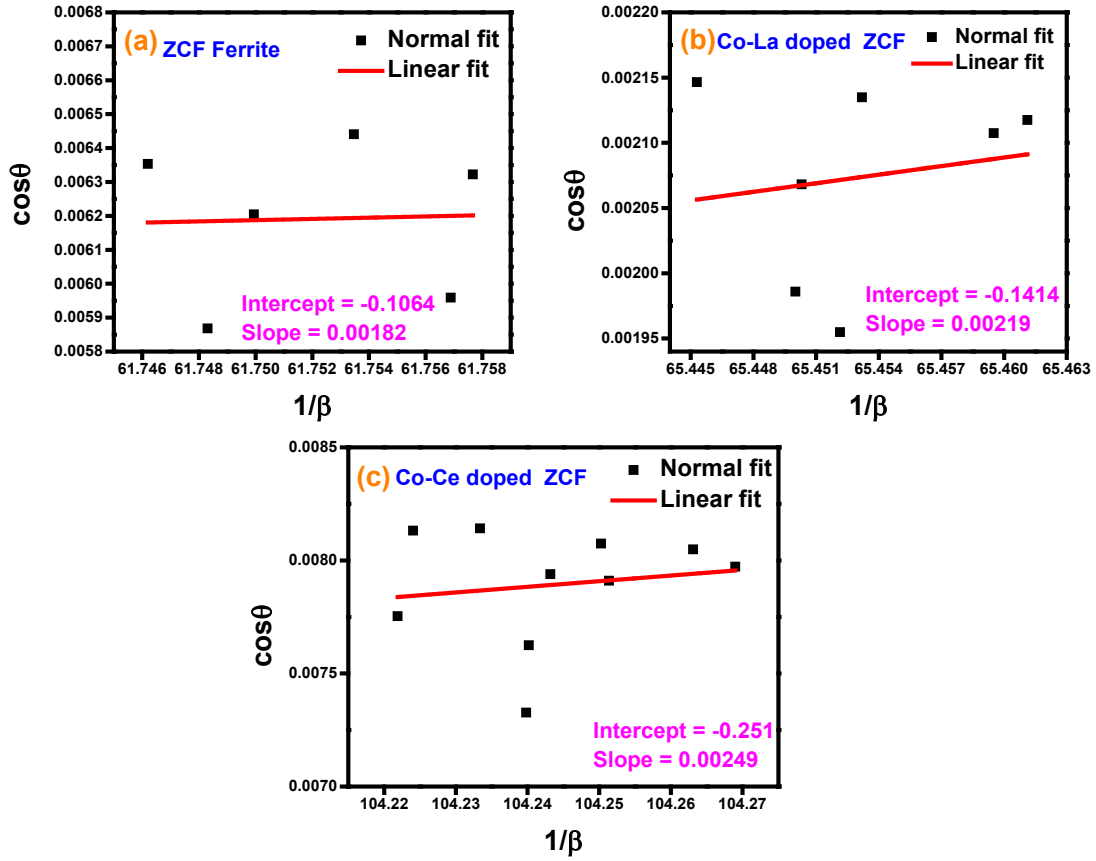


**Fig. 4(a-c)** Scherrer plots for all the ferrite samples

Williamson-Hall (W-H) method was used to calculate crystallite size along with lattice strain, which can be explained the impact of induced strain on peak broadening [30]. According to the W-H method, the total peak broadening is the sum of the size and strain of nano-ferrites. We can write as:

$$\beta = \beta_{\text{size}} + \beta_{\text{strain}} \quad (3)$$

Therefore,

$$\beta = \frac{0.9\lambda}{D} \times \frac{1}{\cos\theta} + 4\epsilon \tan\theta \quad (4)$$

On rearranging the equation (5) we get,

$$\beta \cos\theta = \epsilon (4\sin\theta) + \frac{0.9\lambda}{D} \quad (5)$$

**Fig.5(a-c)** indicates the plotting of the equation (5), with  $4\sin\theta$  along the x-axis and  $\beta \cos\theta$  along the y-axis attributed to XRD peak for the as-prepared ferrite samples. The intercept of the straight line used to determine the average crystallite size and slope provides the lattice strain produced during crystal growth. The origin of strain in the crystal matrix is due to lattice contraction, or extension mainly corresponds to size confinement as compared to bulk counterpart [31]. The average crystallite size calculated from the W-H plot is given in [Table 3](#).

It can be seen from [Table 3](#) that the average crystallite size decreased with the substitution of Co-La and Co-Ce cations. It was also observed that the lattice strain calculated from the W-H plot is also given in [Table 3](#).

W-H method describes the peak broadening as a function of diffraction Bragg's angle, which is considered as a combined impact of size and strain-induced broadening. Size-Strain (SS) plot method described the peak profile in combined Gaussian and Lorentz function. In this method, the lattice strain XRD peak profile is labeled by a Gaussian function, and the crystallite size peak profile is designated as a Lorentz function [32]. We can write a total peak broadening as:

$$\beta = \beta_L + \beta_G \quad (7)$$

where  $\beta_L$  is peak broadening due to Lorentz function and  $\beta_G$  is peak broadening due to Gaussian function. SS plot method provides good results for isotropic nature nano-crystals broadening and lower angle reflection as compared to higher angle reflection with greater accuracy and precision. The reason is that at higher diffracting angles, XRD peaks are overlapped and of low quality. The SS plot calculation is achieved via the following relation [32]:

$$(d\beta \cos\theta)^2 = \frac{k\lambda}{D} (d^2\beta \cos\theta) + \frac{\varepsilon^2}{4} \quad (8)$$

[Fig.6\(a-c\)](#) shows the plots of  $(d^2\beta \cos\theta)$  and  $(d\beta \cos\theta)^2$  for all the as-prepared ferrite samples. The slope of the SS plot is used to find out the crystallite size and intercept to calculate the lattice strain. The crystallite size calculated from the SS plot decreased from 72.94 nm to 48.29 nm with the substitution of dopant cations and lattice strain obtained from the SS plot are also given in [Table 3](#). The dislocation line density ( $\delta$ ) was enhanced with the reduction in the crystallite size ( $D$ ) [33]. The dislocation line density ( $\delta$ ) of the as-prepared ferrites powder increased from  $1.42 \times 10^{-4}$  to  $2.81 \times 10^{-4} \text{ nm}^{-2}$  with the addition of dopants and are listed in [Table 3](#).

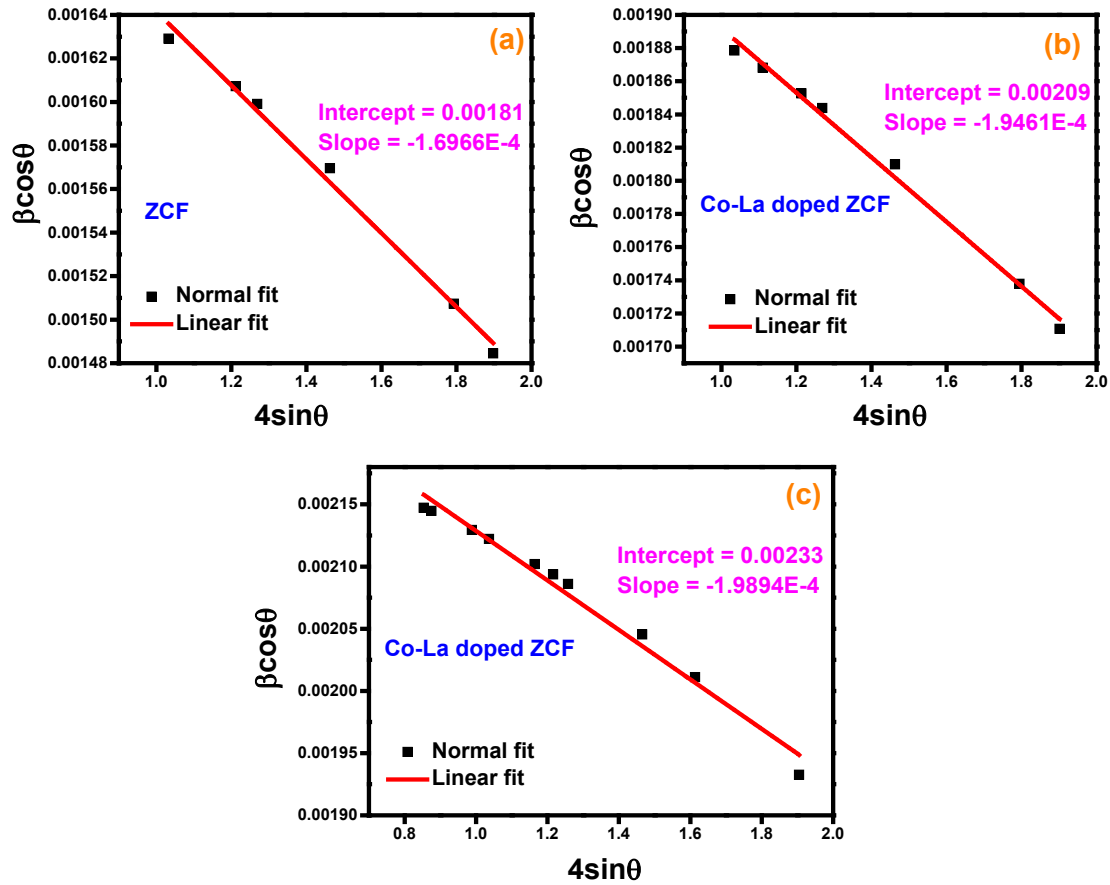


Fig. 5(a-c) W-H plots for all the ferrite samples

Table 3 Comparative crystalline size, strain, and dislocation line density

Samples	Average crystallite size D (nm)				Strain $\epsilon$		Dislocation line density $\delta \times 10^{-4}$ (nm <sup>-2</sup> )
	Scherrer formula	Scherrer plot	Williamson-Hall plot	Size-Strain plot	Williamson-Hall plot	Size-Strain plot	From Scherrer formula
ZCF	83.8	76.15	76.57	72.94	$-1.696 \times 10^{-4}$	$1.164 \times 10^{-5}$	1.42
Co-La doped ZCF	64.9	63.28	66.31	55.66	$-1.946 \times 10^{-4}$	$9.809 \times 10^{-6}$	2.36
Co-Ce doped ZCF	59.7	55.66	59.48	48.29	$-1.989 \times 10^{-4}$	$1.115 \times 10^{-5}$	2.81

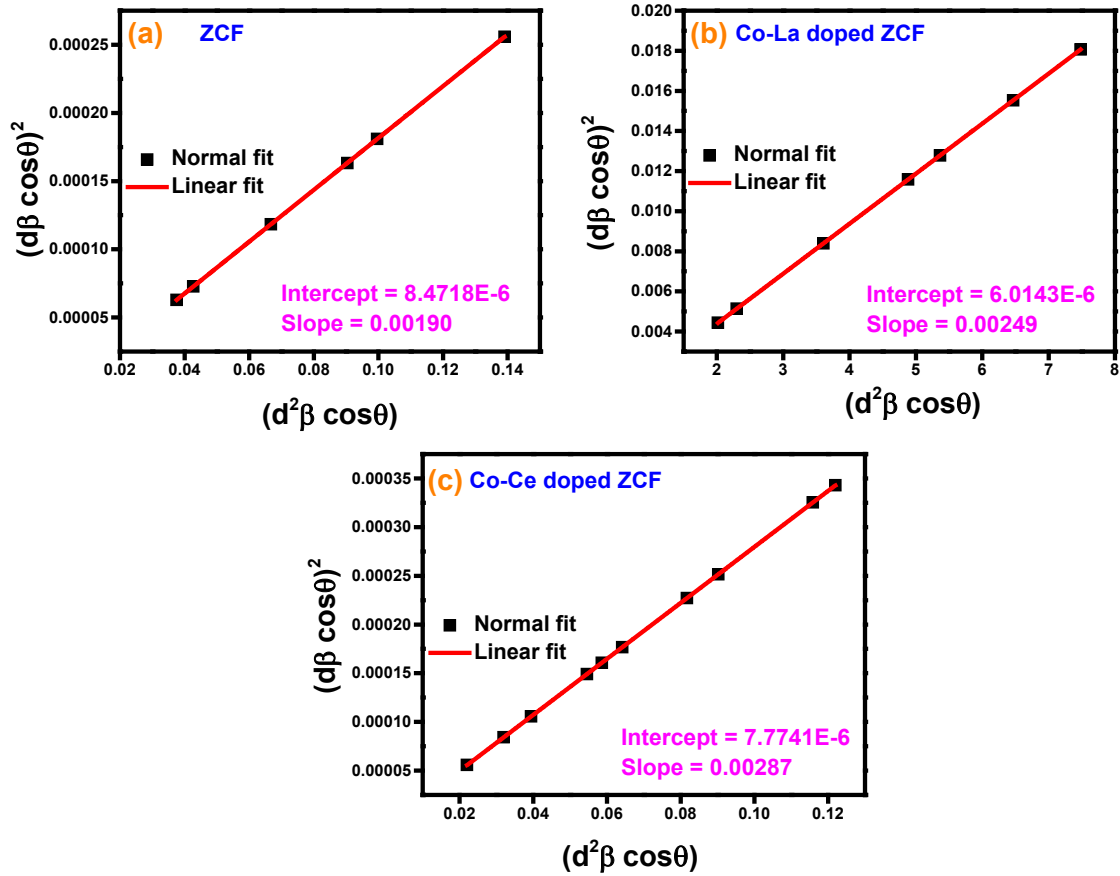


Fig. 6(a-c) Size-strain plots for all the ferrite samples

### 3.1.3 Different XRD parameters

The X-ray density ( $\rho_x$ ) [34], theoretical density ( $\rho_B$ ) [34], relative density ( $\rho_R$ ) [35] and porosity ( $P$ ) [9] of the samples are reported in Table 4. The porosity calculated is in the range that is most desirable and feasible for applications. The graphical variation of the X-ray ( $\rho_x$ ), theoretical ( $\rho_B$ ), relative density ( $\rho_R$ ) and porosity percentage are shown in Fig. 7. The “ $\rho_x$ ” and “ $\rho_B$ ” were observed to reduce with the substitution of dopant cations as compared to the pure Zn-Cu ferrite. This reduction in densities may be due to the greater radii of the dopant cations [35].

The determined values of specific surface area ( $S$ ) and packing factor ( $p$ ) of all the synthesized nano ferrite samples are listed in Table 4. It is clear from Table 4 that the packing factor ( $p$ ) decreased with the substitution of the dopant cations. The specific surface area ( $S$ ) was found to have an increasing trend with the substitution of dopant ions as compared to the pure ZCF sample. Due to the creation of polaron (electron-phonon interactions), the charge carriers are not free in the spinel structure nano ferrites but are highly localized in their d-shells. A slight polaron defect is produced as a result of the displacement of neighboring atoms or ions

when a charge carrier is trapped at a given lattice site [36]. It was found from Table 4 that the determined polaron radius ( $\gamma_p$ ) was reduced with the addition of dopant ions and has a minimum value of 0.7525 Å for the Co-Ce substituted ZCF sample. This suggests that the electric charge carriers required less energy from one cationic lattice site to another with the addition of dopant ions ( $\text{Co}^{2+}$ ,  $\text{La}^{3+}$ , and  $\text{Ce}^{3+}$ ). Tetrahedral ( $A$ -) site hopping length  $H_A$  and octahedral ( $B$ -) site hopping length  $H_B$  were calculated [37] and are listed in Table 4. It was found from Table 4 that the hopping length decreased with the dopant's inclusion. This behavior of  $A$ - site hopping length " $H_A$ " and  $B$ - site hopping length " $H_B$ " is analogous with the behavior of lattice constant ( $a$ ). It may be due to the difference in ionic radii of the constituent cations [38]. The plot of polaron radius ( $\gamma_p$ ), hopping length  $H_A$ , and  $H_B$  versus ZCF, Co-La doped ZCF, and Co-Ce substituted ZCF samples is shown in Fig. 8.

**Table 4:** X-ray ( $\rho_x$ ), bulk ( $\rho_B$ ) and relative ( $\rho_R$ ) densities, porosity ( $P$ ) percentage, packing factor ( $p$ ), strain ( $\epsilon$ ), specific surface area ( $S$ ), and polaron radius ( $\gamma_p$ ) for nano ferrites samples

Samples	$\rho_x$ (g/cm <sup>3</sup> )	$\rho_B$ (g/cm <sup>3</sup> )	$\rho_R$ (%)	$P$ (%)	$p$	$S$ (cm <sup>2</sup> /g)	$\gamma_p$ (Å)	$H_A$ (Å)	$H_B$ (Å)
ZCF	5.31	3.29	161.33	38.02	329.88	0.0135	0.7546	3.6487	2.9788
Co-La doped ZCF	5.56	4.71	118.24	15.43	256.24	0.0165	0.7532	3.6420	2.9733
Co-Ce doped ZCF	5.59	4.98	112.23	10.89	235.58	0.0179	0.7525	3.6384	2.9704

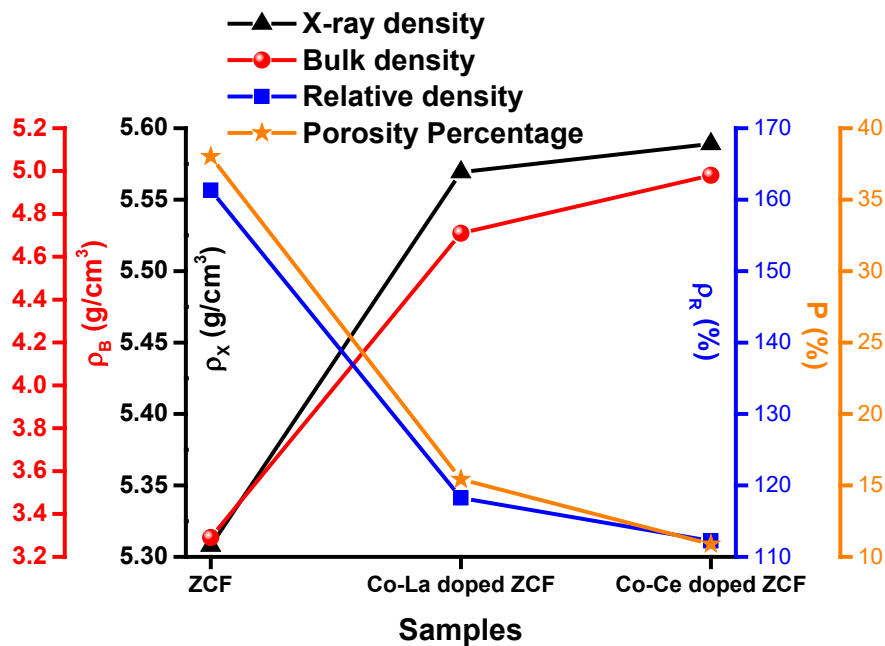


**Fig. 7** Graphical representation of X-ray density ( $\rho_x$ ), theoretical density ( $\rho_B$ ), theoretical density ( $\rho_R$ ) and porosity ( $P$ ) as-prepared nano ferrites

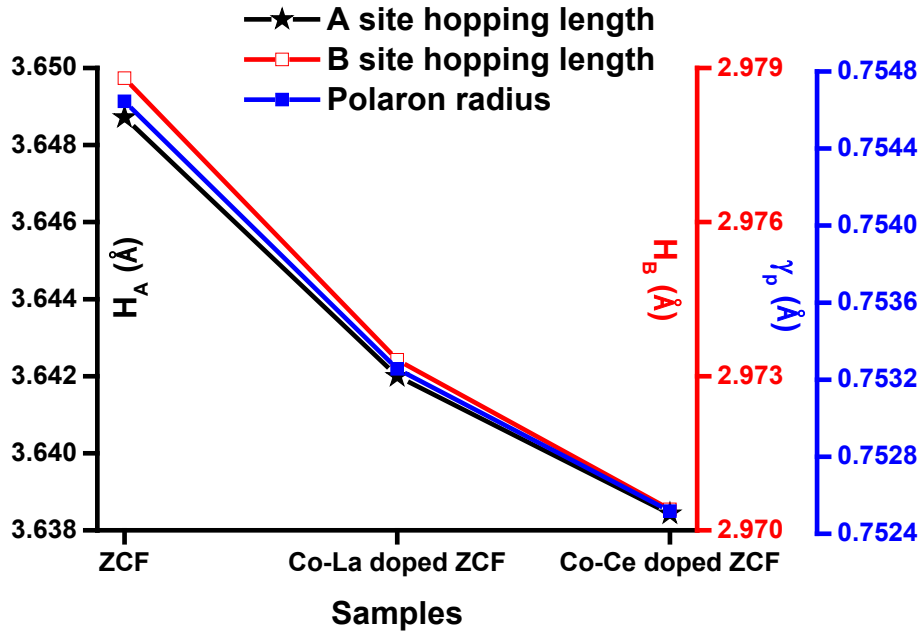


**Fig. 8** Graphical representation of hopping length and polaron radius of as-prepared samples

### 3.2 Absorption band analysis

The absorption bands are around  $(558.87 - 577.82) \times 10^2 \text{ m}^{-1}$  with slight differences among the prepared nano ferrites. They depend on the bond strength and length, which could be due to stretching vibrations of the tetrahedral groups  $\text{Fe}^{3+} - \text{O}^{2-}$  and  $\text{Me}^{2+}$  ( $\text{Zn}^{2+}$  or  $\text{Co}^{2+}$  or  $\text{Cu}^{2+}$ )  $- \text{O}^{2-}$ ; whereas the bands around  $(418.84 - 420.16) \times 10^2 \text{ m}^{-1}$  are due to the octahedral groups complex  $\text{Fe}^{3+}$  ( $\text{La}^{3+}$  or  $\text{Ce}^{3+}$ )  $- \text{O}^{2-}$  (Fig. 9). Such a difference in the frequency bands at the two sites is due to changes in bond lengths and the site preference of the constituent cations [35]. Thus, the bonding vibrations at the respective sites (i.e., at the tetrahedral and octahedral) at close proximities of the respective wavelengths confirm the formation of the spinel ferrites of the synthesized materials. By using absorption  $\nu_T$  and  $\nu_O$  bands, the force constant for both tetrahedral ( $k_T$ ) and octahedral ( $k_O$ ) sites are calculated using  $k = 4\pi^2\nu^2c^2m$  [39], where “ $c$ ” is the speed of light, “ $\nu$ ” is the wavenumber and “ $m$ ” is the reduced mass for  $\text{Fe}^{3+}$  ions and  $\text{O}^{2-}$  ions ( $2.061 \times 10^{-23} \text{ g}$ ). The values of absorption  $\nu_T$  and  $\nu_O$  bands and force constant for tetrahedral ( $k_T$ ) and octahedral ( $k_O$ ) sites are listed in Table 5. The difference between  $\nu_T$  and  $\nu_O$  band positions may be due to the difference in bond strength and distance of metal-oxygen ions at various sites of the crystal structure, which are modified when dopant cations are replaced with  $\text{Fe}^{3+}$  cations. This may be retained to the shorter bond length of metal-oxygen in the A site than that in the B site [39].

The average force constant ( $k_{av}$ ) was determined via  $k_{av} = (k_T + k_O)/2$  and the stiffness constants were calculated using the following relations  $C_{11} = k_{av}/a$ , where “ $a$ ” is a lattice

constant and  $C_{12} = \sigma C_{11} / (1 - \sigma)$  [40], where “ $\sigma$ ” is a Poisson ratio [ $\sigma = 0.324(1 - 1.04P)$ ], where “ $P$ ” is a porosity fraction [40]. The variation in the average force constant ( $k_{av}$ ), stiffness constants ( $C_{11}$  and  $C_{12}$ ) and Poisson ratio ( $\sigma$ ) are reported in Table 5. The stiffness constants ( $C_{11}$  and  $C_{12}$ ) increased with the addition of the dopant cations in the ZCF sample as compared with the pure ZCF sample. This may be due to the lattice constant decreasing and the average force constant ( $k_{av}$ ) increasing [41]. The Poisson ratio ( $\sigma$ ) of our as-prepared samples lies between 0.19 and 0.29, which conforms to isotropic elasticity theory where the Poisson ratio ( $\sigma$ ) lies in the range of -1 to 0.5 [41].

The different elastic parameters measured are significant for homogeneous and isotropic spinel matrix nano ferrites. The bulk ( $B$ ), Young’s ( $E$ ), and rigidity ( $G$ ) moduli were determined using the following relations  $B = 1/3[C_{11} + 2C_{12}]$ ,  $E = 3(C_{11} - C_{12}) B / (C_{11} + C_{12})$  and  $G = E/2(\sigma + 1)$  [40] and the values of elastic parameters are reported in Table 5.

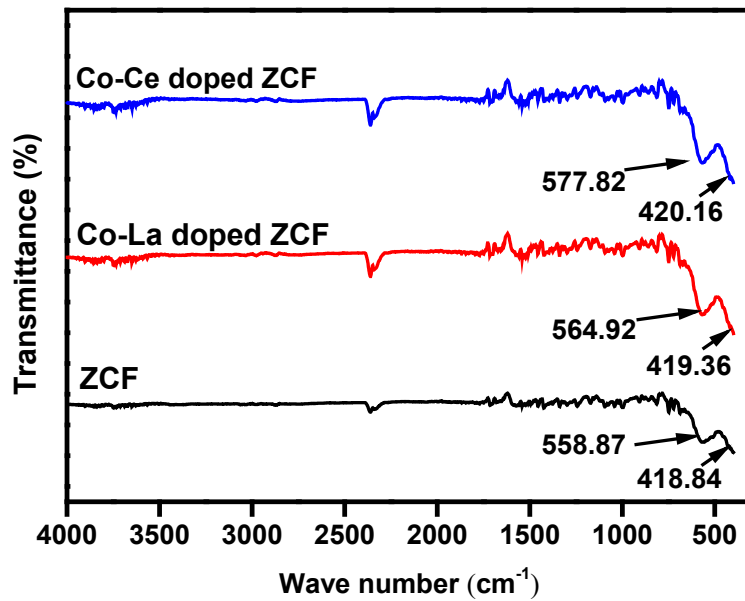


Fig. 9 Absorption bands spectra for as-prepared ferrite samples

Table 5: Absorption bands, force constant, and different mechanical parameters for as-prepared samples

Samples	$\nu_T$	$\nu_0$	$k_T$	$k_0$	$k_{av}$	$\sigma$	$C_{11}$	$C_{12}$	$B$	$E$	$G$
	$10^2 \times (\text{m}^{-1})$		$(\text{N/m})$		$(\text{G Pa})$						
ZCF	558.87	418.84	288.64	162.12	225.38	0.19	267.47	65.01	132.48	242.02	101.22
Co-La doped ZCF	564.92	419.36	294.92	162.52	228.72	0.27	271.93	101.53	158.31	216.71	85.19
Co-Ce doped ZCF	577.82	420.16	308.55	163.15	235.85	0.29	280.67	113.09	168.92	215.71	83.79

### 3.3 Optical band gap analysis

The optical band gap in spinel structure nano ferrites depends on the following factors: the structure parameters, lattice strains, particle size, dopant concentration, presence of an impurity, and surficial effects [42]. The absorption coefficient ( $\alpha$ ) was calculated using the formula  $\alpha = 2.303 \log(A)$  [35], where “A” represents the absorbance. The optical band gap ( $E_g$ ) was calculated via the following relation  $(\alpha h\nu)^2 = B(E_g - h\nu)$  [35], where  $h\nu$  and  $B$  represent the energy of photons and transition probability dependence constant. Tauc plots [9] were employed for the as-prepared pure ZCF and dopant ( $\text{Co}^{2+}$ ,  $\text{La}^{3+}$ , and  $\text{Ce}^{3+}$ ) cations doped ZCF samples as shown in Fig. 10(a-c). The optical band gap ( $E_g$ ) increased with the addition of dopant cations when compared to the pure ZCF sample. The maximum optical band gap ( $E_g$ ) was 2.99 eV for the Co-Ce doped ZCF sample (depicted in Fig. 10(a-c)).

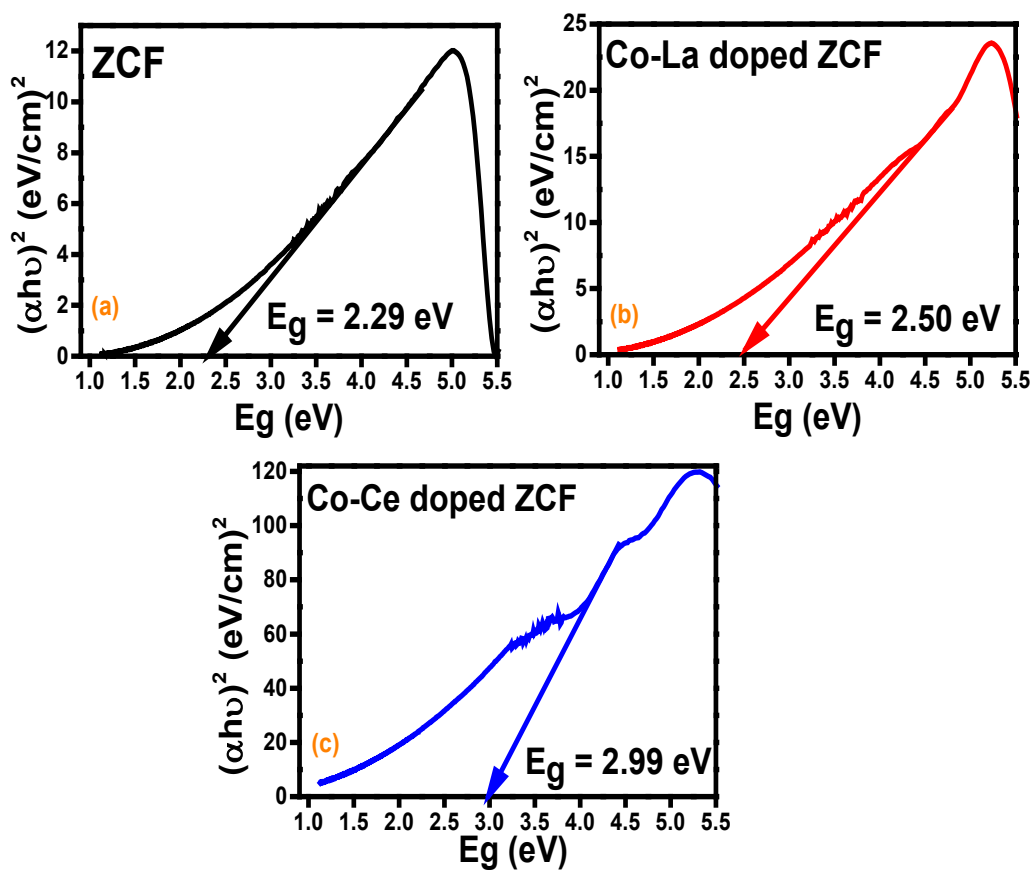


Fig. 10(a-c) Tauc plots for pure and doped ZCF samples

### 3.4 Current Voltage ( $I$ - $V$ ) measurement analysis

Arrhenius plots for pure ZCF and cations ( $\text{Co}^{2+}$ ,  $\text{La}^{3+}$ , and  $\text{Ce}^{3+}$ ) doped ZCF samples i.e., log of resistivity ( $\log \rho$ ) and the inverse of temperature ( $1000/T$ ) are shown in Fig. 11. The change in the slope of the curve for the resistivity splits the curve into two regions correlating

to the ferromagnetic region and paramagnetic region. The variation in resistivity is linear up to a temperature, where a kink appears called the transition temperature or the Curie temperature ( $T_C$ ). This leads to the conversion of magnetic ordering to paramagnetism from ferromagnetism. Hence the plots consist of two regions, below " $T_C$ " is called the ferromagnetic region while above " $T_C$ " is called the paramagnetic region [9]. It was found that the DC resistivity ( $\rho$ ) increased with addition of dopant cations ( $\text{Co}^{2+}$ ,  $\text{La}^{3+}$ , and  $\text{Ce}^{3+}$ ) as compared to the pure ZCF sample. This may be because different types of conducting channels are present in the as-prepared spinel ferrites for electrons hopping such as  $\text{Fe}^{3+}\text{-Fe}^{3+}$  and  $\text{Fe}^{3+}\text{-Metal ion}$  ( $\text{Zn}^{2+}$ ,  $\text{Cu}^{2+}$ ,  $\text{Co}^{2+}$ ,  $\text{La}^{3+}$ , and  $\text{Ce}^{3+}$ ), which are responsible for the modification of electrical properties [9]. It can be observed from Fig. 12(a) that the electrical resistivity ( $\rho$ ) at different temperatures such as 303 K, 423 K, 473 K, 523 K, 573 K, 623 K has a maximum value for Co-Ce substituted ZCF sample. The activation energy ( $\Delta E$ ) is calculated by taking the slope of  $\log \rho$  versus  $1000/T$  using the following relation  $\Delta E = 2.303 \times k_B \times 1000 \times \text{slope (eV)}$  [39], where  $k_B$  is Boltzmann constant ( $8.602 \times 10^{-5}$  eV/K). The calculated values and the behavior of activation energy ( $\Delta E$ ) for as-synthesized samples are depicted in Fig. 12(b). The activation energy ( $\Delta E$ ) increased with the addition of cations ( $\text{Co}^{2+}$ ,  $\text{La}^{3+}$ , and  $\text{Ce}^{3+}$ ) in ZCF and has a maximum value for Co-Ce substituted ZCF sample.

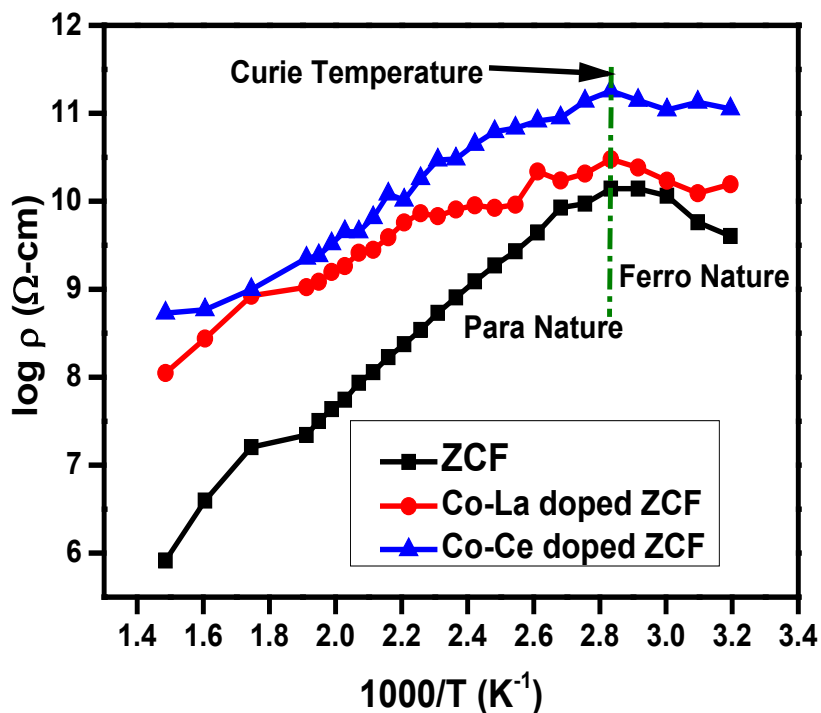
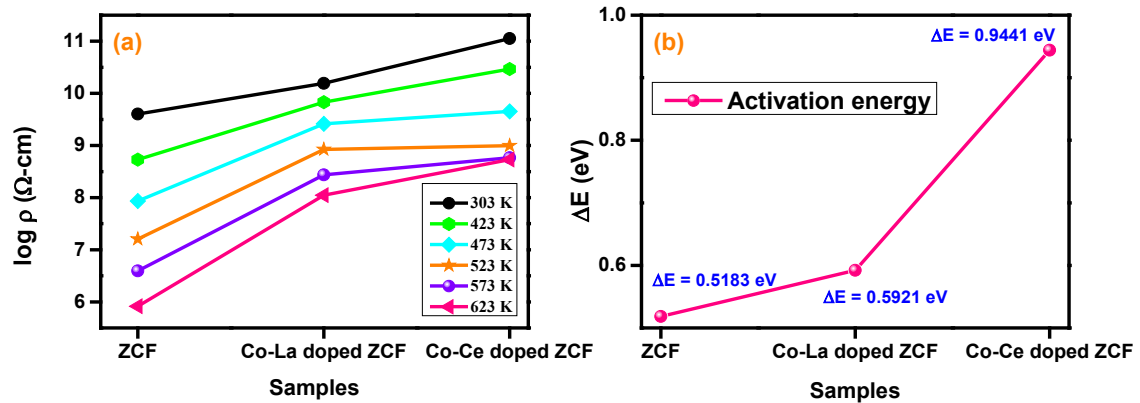


Fig. 11 Arrhenius plots for pure and cations ( $\text{Co}^{2+}$ ,  $\text{La}^{3+}$ , and  $\text{Ce}^{3+}$ ) doped ZCF samples



**Fig. 12** Samples *versus* (a) log of resistivity at various temperatures (b) activation energy

### 3.5 Dielectric measurement analysis

The dielectric parameters were measured within the frequency range of 8 Hz to 8 MHz at 303 K. The dependence of the dielectric constant with the frequency variation is shown in Fig. 13(a). It is revealed that the dielectric constant decreased with the increment of applied frequency and ultimately maintained a constant value for higher frequencies. The dielectric constant reduced very rapidly at small, applied frequencies, but it reduced very slowly for the higher frequencies. This may be due to the electrons hopping between different conducting channels ions [43].

It is clear from Fig. 13(b) that the tangent loss ( $\tan \delta$ ) has a high value when the frequency was in the lower range, on the other hand at high-frequencies, the polarization decreased and loss tangent became continuous. In the case of ferrites, the conduction mechanism can be correlated with changes in tangent loss with the change of frequency, similar to Koop's model [43]. It was also observed from Fig. 14 that the tangent loss ( $\tan \delta$ ) increased with the substitution of cations ( $\text{Co}^{2+}$ ,  $\text{La}^{3+}$ , and  $\text{Ce}^{3+}$ ) and maximum tangent loss was found for the Co-Ce doped ZCF sample.

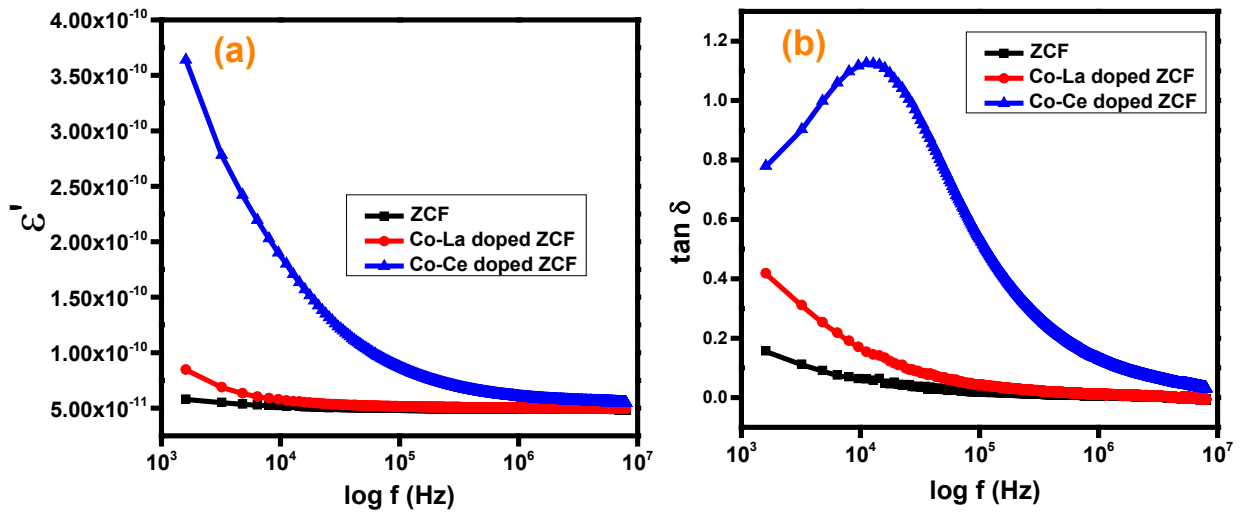


**Fig. 13** Plots of (a) dielectric constant *versus* the *log* of frequency (b) tangent loss *versus* the *log* of frequency at 303 K

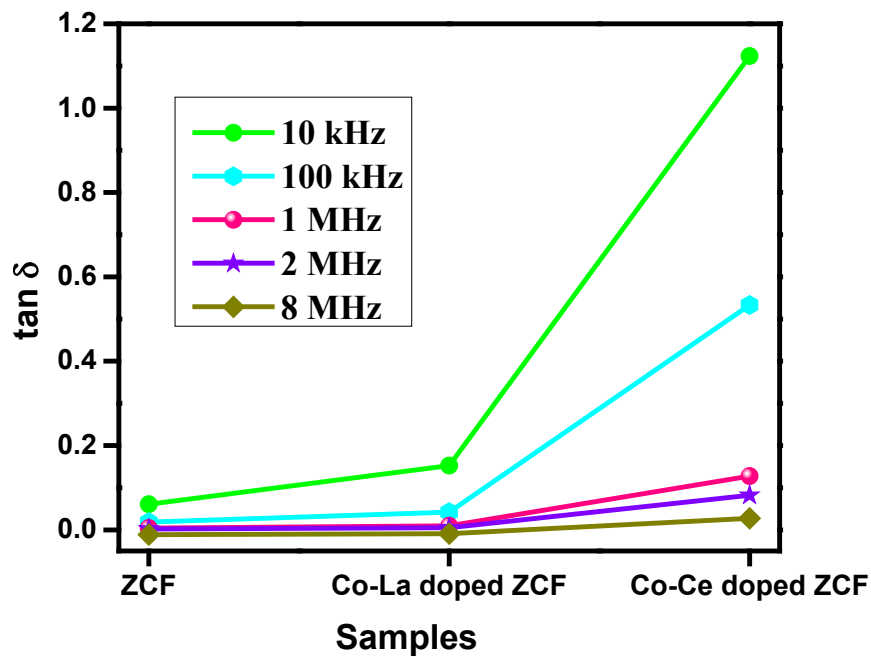


**Fig. 14** Plots of tangent loss at different frequencies for as-prepared samples

### 3.6 Magnetic properties analysis

The  $M$ - $H$  hysteresis loops for all the ferrite samples at 303 K are shown in Fig. 15(a-c). The S-shaped  $M$ - $H$  loops denoted that the as-prepared spinel matrix nano ferrites have a soft magnetic nature. The observed values Coercivity ( $H_c$ ), Magnetization ( $M_s$ ), Retentivity ( $M_r$ ), squareness ratio ( $R = M_r/M_s$ ) [44], magneto crystalline anisotropy constant ( $K$ ) [44], and

microwave frequency ( $\omega_m$ ) are listed in Table 6. The Coercivity ( $H_C$ ) has the maximum value for the Co-Ce doped ZCF sample. The remnant magnetization ( $M_r$ ) and saturation magnetization ( $M_s$ ) indicate the same behavior as coercivity ( $H_C$ ). It was found from the literature study that the magnetic parameters decreased with the substitution of rare earth cations, but in the current study of ferrites, it was observed that the Coercivity ( $H_C$ ), Saturation Magnetization ( $M_s$ ), and Retentivity ( $M_r$ ) increased with the substitution of dopant cations ( $\text{Co}^{2+}$ ,  $\text{La}^{3+}$ , and  $\text{Ce}^{3+}$ ). It may be due to the insertion of  $\text{Co}^{2+}$  cation along with  $\text{La}^{3+}$  and  $\text{Ce}^{3+}$  cation in ZCF samples. Because  $\text{Co}^{2+}$  replaced  $\text{Zn}^{2+}$  in the as-prepared samples and this substitution is responsible for the increasing trend of magnetic parameters [45].

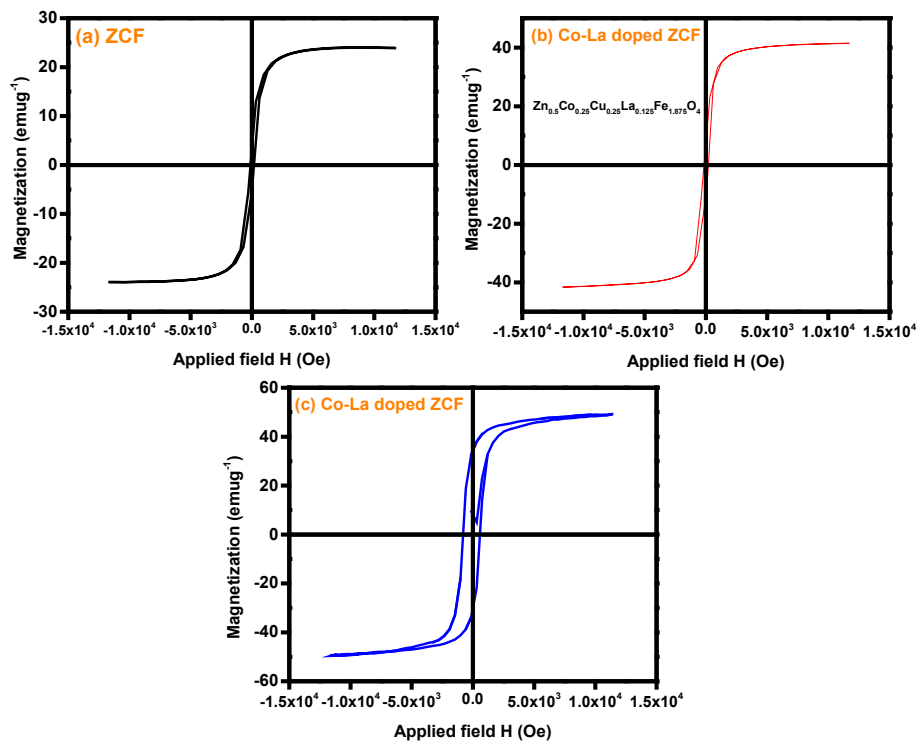


**Fig. 15(a-b)** Room temperature  $M$ - $H$  loop for pure and cations ( $\text{Co}^{2+}$ ,  $\text{La}^{3+}$ , and  $\text{Ce}^{3+}$ ) doped ZCF samples

The squareness ratio ( $R$ ) increased from 0.1295 to 0.6976 with the substitution of dopant cations ( $\text{Co}^{2+}$ ,  $\text{La}^{3+}$ , and  $\text{Ce}^{3+}$ ) and the calculated squareness ratio ( $R$ ) was less than unity, which indicates the superparamagnetic behavior of the as-prepared spinel ferrites [46]. The anisotropy constant ( $K = H_C \times M_s / 0.96$ ) was calculated and is given in Table 6. The value of the anisotropy constant increased with the substitution of dopant cations as compared with the pure ZCF sample and has a maximum for the Co-Ce doped ZCF sample. The microwave frequency ( $\omega_m$ ) determined using relation  $\omega_m = 8\pi^2 M_s \gamma$ , where “ $\gamma$ ” is a gyromagnetic fraction with the significance of 2.8 MHz/Oe, and  $M_s$  saturation magnetization [47, 48]. The applied

field *versus* microwaves operating frequency ( $\omega_m$ ) of the as-prepared ferrites samples is plotted in Fig. 16(a-c). It can be found from Fig. 16(a-c) that the range of microwaves operating frequency ( $\omega_m$ ) is 5.31 – 10.91 GHz, which indicates that the as-prepared nano ferrites are applicable in longitudinal recording media and microwave absorbance purposes.

**Table 6** Magnetic parameters for all the as-prepared samples

$x$	$H_c$ ( $\pm 0.01$ ) (Oe)	$M_r$ ( $\pm 0.01$ ) (emu/g)	$M_s$ ( $\pm 0.01$ ) (emu/g)	$R$	$K$ (erg/cm <sup>3</sup> )	$\omega_m$ (GHz)	$H_m$ (Oe)	$\chi = dM/dH$ (emu/g Oe)	
								H $\rightarrow$ 0	H $\rightarrow$ $H_m$
ZCF	128.36	3.14	24.25	0.1295	3242.43	5.31	292.41	0.018	0.024
Co-La doped ZCF	157.31	6.98	41.43	0.1685	6788.91	9.21	341.99	0.035	0.043
Co-Ce doped ZCF	813.71	34.31	49.18	0.6976	41685.68	10.91	641.54	0.041	0.061

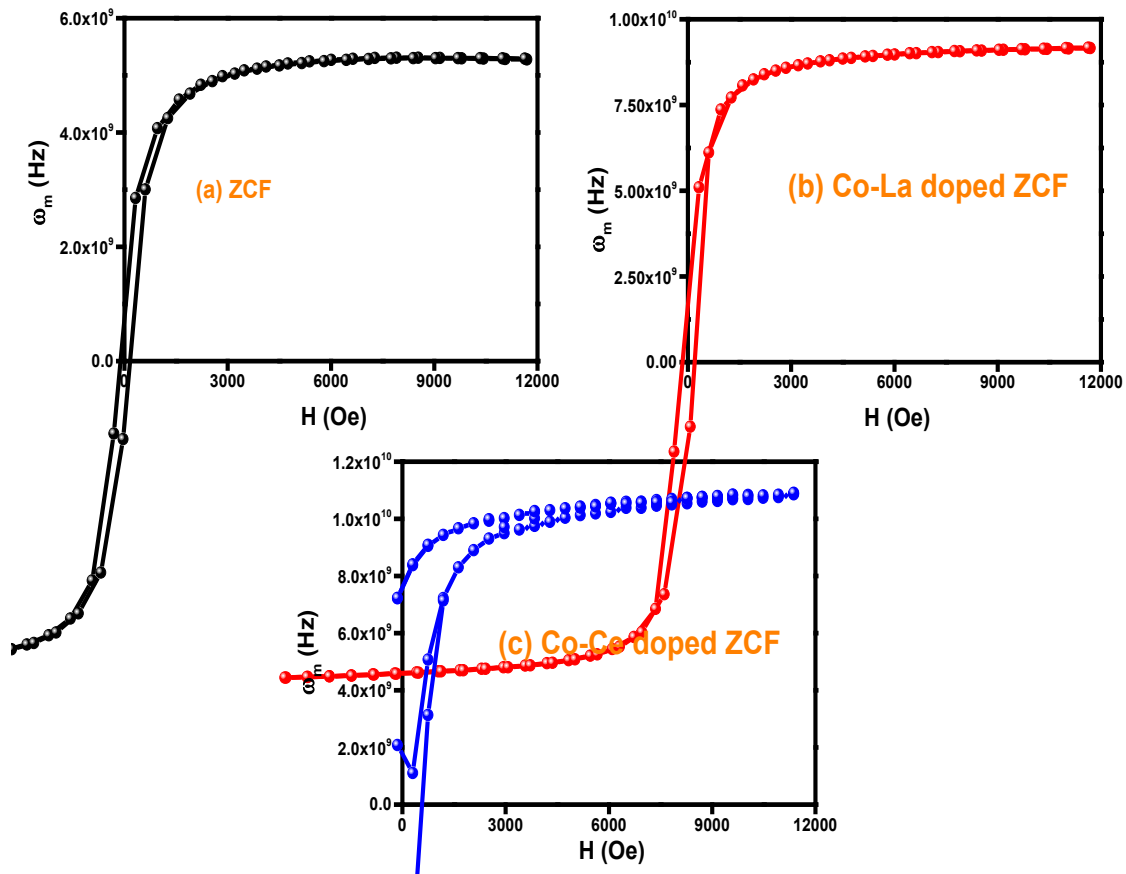


**Fig. 16** Applied field *versus* microwaves operating frequency

Fig. 17(a-c) showed field dependence of  $dM/dH$  curve at 303 K used for study the impact of a single domain (SD)/pseudo-single domain (PSD) and multi-domain (MD) behavior

of the grains in pure and cations ( $\text{Co}^{2+}$ ,  $\text{La}^{3+}$ , and  $\text{Ce}^{3+}$ ) substituted ZCF samples [49]. The term  $dM/dH$  is known magnetic susceptibility ( $\chi$ ) of the ferrite samples. The magnetic susceptibility ( $\chi = dM/dH$ ) is technically significant (infinite) in the case of ideal domain nanoparticles with a square  $M-H$  curve at the coercive field ( $H_c$ ) and is zero as  $H \rightarrow 0$ . The finite values of  $\chi = dM/dH$  at  $H \rightarrow 0$  are reported in Table 6 confirms the SD/PSD and MD grains regimes in the as-prepared ferrites. The  $dM/dH$  versus  $H$  curves (Fig. 17(a-c)) indicate the peak at  $\sim H_m$ . The observed peaks are separated by  $2H_m$  and symmetric around  $H \rightarrow 0$ . The observed values of  $H_m$  and  $dM/dH$  at  $H \rightarrow H_m$  are listed in Table 6. The greater values of  $H_m$  as compared to  $H_c$  represent the switching field distribution (SFD) because of disordered shell contribution in PSD or MD grains [50]. The values of the peak height of magnetic susceptibility ( $\chi = dM/dH$ ) at  $H_m$  are given in Table 6. It was observed that the values of  $\chi = dM/dH$  at  $H \rightarrow H_m$  are greater than at  $H \rightarrow 0$ . The increasing peak separation, as well as peak height of  $\chi = dM/dH$  at  $H_m$ , shows a magnetically well stable state and good crystallization cubic matrix of all the samples. On the other hand, the narrow peak separations and small peak height for the nano ferrites are owing to the existence of huge unstable superparamagnetic domains [51].

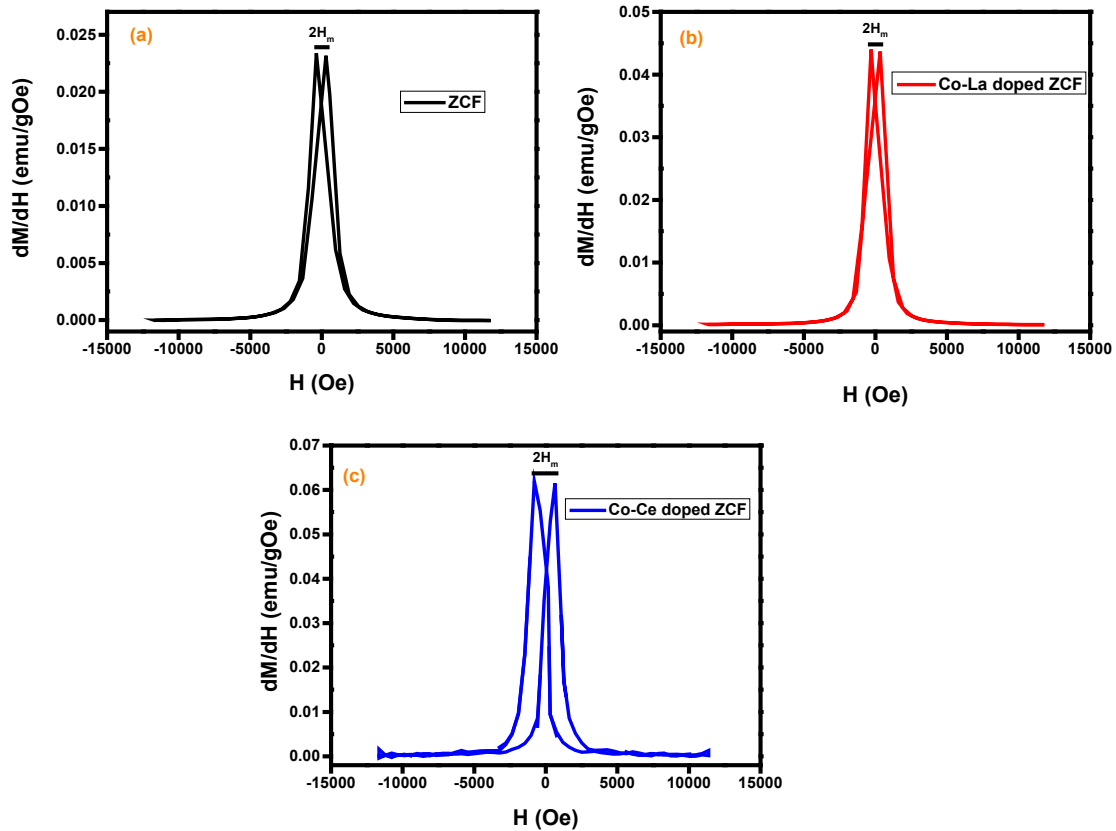


Fig. 17(a-c) Field dependence for all the as-synthesized ferrite samples

### 3.7 Morphological Analysis

SEM was used for the morphological analysis of the as-prepared ZCF and Co-La doped ZCF samples. Fig. 18(a-b) indicated that the micrographs of the as-synthesized ferrites at the scale of 500 nm (and at 100000 × magnifications). The micrographs of the ZCF and Co-La doped ZCF sample powder revealed an irregular particle shape and size. Fig. 18(a) showed that the average particle size of the ZCF sample is 479.1 nm and Fig. 18(b) indicated that the average particle size for Co-La doped ZCF sample is 391.2 nm. It was found that the particle size decreased as we doped the ZCF sample with the Co-La cations. High calcination temperatures induce particle agglomeration due to various emerging forces including weak Van der Waals, electrostatic, and capillary forces, all of which create magnetic interactions between the particles [9]. Therefore, it was observed the particle agglomeration in the as-prepared ZCF and Co-La doped ZCF samples.

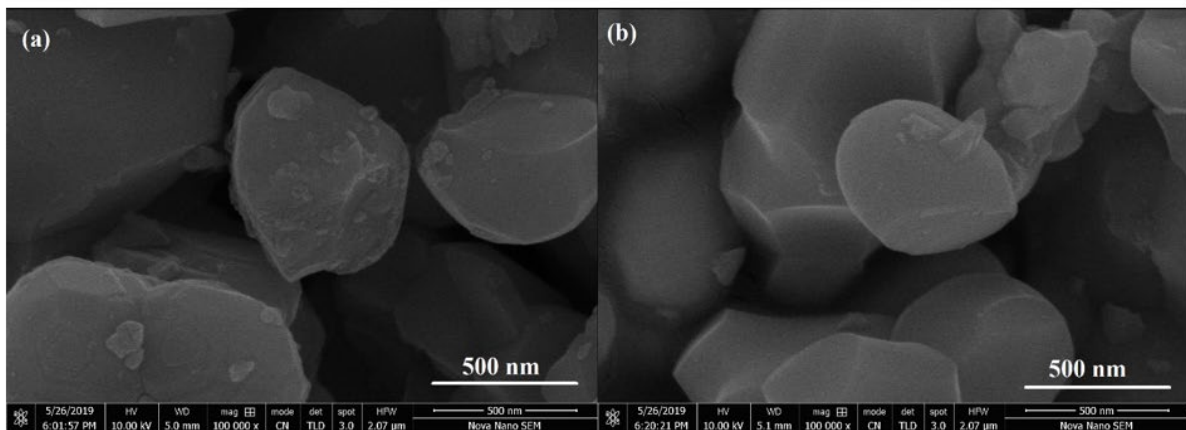


Fig. 18(a-b) SEM images of the as-prepared samples

### 3.8 Chemical Composition Analysis

The chemical composition of the as-prepared samples was confirmed by EDX analysis and is depicted in Fig. 19(a-b). The analysis confirmed that the existence of Zn, Cu, Fe, and O elements in the ZCF sample (Fig. 19(a)) and Zn, Cu, Fe, Co, La, and O elements in the Co-La doped ZCF sample (Fig. 19(b)). The presence of oxygen is a necessary element in the composition of as-prepared ferrite samples. The results revealed that the as-prepared samples did not contain any raw element and the experimental values of composition close to the theoretical values of chemical composition.

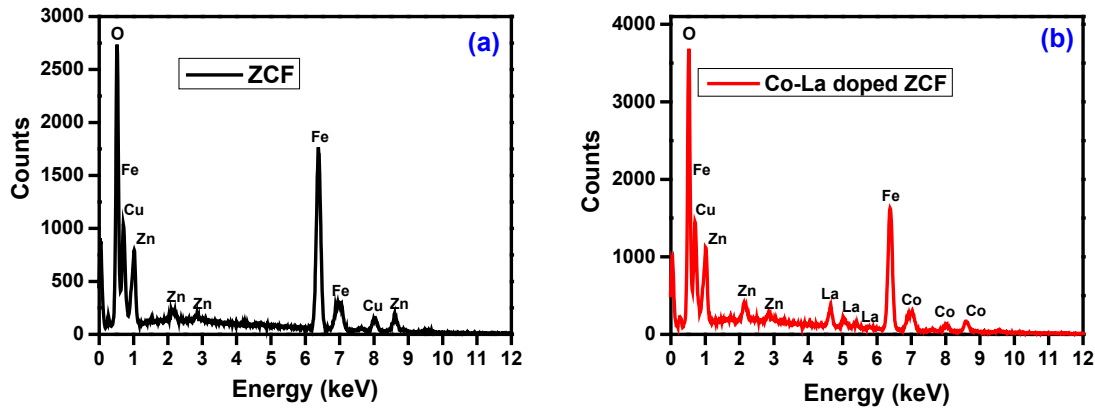


Fig. 19(a-b) Composition pattern for ZCF and Co-La substituted ZCF samples

## 4 Conclusions

Sol-gel auto-igniting route used for the synthesis of ZCF, Co-La substituted ZCF, and Co-Ce doped ZCF samples powder. Rietveld refinement confirmed the formation of spinel cubic matrix and the lattice constant ( $a$ ) was reduced with the insertion of dopant cations. Moreover, the crystallite size ( $D$ ) was also reduced determined *via* different methods. The variation in the low-frequency absorption bands confirmed the substitution of dopant cations at the octahedral site. The energy bandgap ( $E_g$ ), activation energy, and resistivity ( $\rho$ ) had the maximum value for the Co-Ce doped ZCF sample. The dielectric constant was reduced with the increase of applied frequency and for higher values of the frequency ultimately dielectric constant remains constant. The minimum tangent loss was observed for the ZCF sample. The maximum Coercivity ( $H_C$ ) was 813.71 Oe for the Co-Ce doped ZCF sample. The remnant magnetization ( $M_r$ ) and saturation magnetization ( $M_s$ ) have also maximum values for the Co-Ce doped ZCF sample. The squareness ratio ( $R$ ) increased from 0.1295 to 0.6976 with the substitution of dopant cations. Overall, the magnetic stability of the samples was confirmed by the increased peak height of  $dM/dH$  at  $H_m$  and the separation between the peaks. Micrographs indicate that the irregularity in size and shape of the particles. The chemical composition analysis revealed that the experimental values are close to the theoretical values.

## References

- [1] S. Nasrin, F.U.Z. Chowdhury, S. Hoque, Study of hyperthermia temperature of manganese-substituted cobalt nano ferrites prepared by chemical co-precipitation method for biomedical application, *Journal of Magnetism and Magnetic Materials*, 479 (2019) 126-134.
- [2] F. Gheorghiu, R. Stanculescu, L. Curecheriu, E. Brunengo, P. Stagnaro, V. Tiron, P. Postolache, M.T. Buscaglia, L. Mitoseriu, PVDF–ferrite composites with dual magneto-piezoelectric response for flexible electronics applications: synthesis and functional properties, *Journal of Materials Science*, 55 (2020) 3926-3939.

- [3] K.K. Kefeni, B.B. Mamba, Photocatalytic application of spinel ferrite nanoparticles and nanocomposites in wastewater treatment, *Sustainable Materials and Technologies*, 23 (2020) e00140.
- [4] M.B. Askari, P. Salarizadeh, Binary nickel ferrite oxide (NiFe<sub>2</sub>O<sub>4</sub>) nanoparticles coated on reduced graphene oxide as stable and high-performance asymmetric supercapacitor electrode material, *International Journal of Hydrogen Energy*, 45 (2020) 27482-27491.
- [5] M. Arifuzzaman, M.B. Hossen, J.D. Afroze, M. Abden, Structural and electrical properties of Cu substituted Ni–Cd nanoferrites for microwave applications, *Physica B: Condensed Matter*, 588 (2020) 412170.
- [6] Z. Zhang, Design and experimental verification of low cost ferrite PM-assisted synchronous reluctance motor, in: 2020 IEEE Transportation Electrification Conference & Expo (ITEC), IEEE, 2020, pp. 327-334.
- [7] M.A. Maksoud, G.S. El-Sayyad, A. Abokhadra, L. Soliman, H. El-Bahnasawy, A. Ashour, Influence of Mg<sup>2+</sup> substitution on structural, optical, magnetic, and antimicrobial properties of Mn–Zn ferrite nanoparticles, *Journal of Materials Science: Materials in Electronics*, 31 (2020) 2598-2616.
- [8] Q. Tan, C. Wang, Y. Cao, X. Liu, H. Cao, G. Wu, B. Xu, Synthesis of a zinc ferrite effectively encapsulated by reduced graphene oxide composite anode material for high-rate lithium ion storage, *Journal of Colloid and Interface Science*, 579 (2020) 723-732.
- [9] A.U. Rehman, N. Morley, N. Amin, M.I. Arshad, M.A. un Nabi, K. Mahmood, A. Ali, A. Aslam, A. Bibi, M.Z. Iqbal, Controllable synthesis of La<sup>3+</sup> doped Zn<sub>0.5</sub>Co<sub>0.25</sub>Cu<sub>0.25</sub>Fe<sub>2-x</sub>La<sub>x</sub>O<sub>4</sub> (x = 0.0, 0.0125, 0.025, 0.0375, 0.05) nano-ferrites by sol-gel auto-combustion route, *Ceramics International*, 46 (2020) 29297-29308.
- [10] N. Tian, H. Huang, Y. He, Y. Guo, T. Zhang, Y. Zhang, Mediator-free direct Z-scheme photocatalytic system: BiVO<sub>4</sub>/gC<sub>3</sub>N<sub>4</sub> organic–inorganic hybrid photocatalyst with highly efficient visible-light-induced photocatalytic activity, *Dalton Transactions*, 44 (2015) 4297-4307.
- [11] M. Hanif, O. Farooq, U. Rafiq, M. Anis-Ur-Rehman, A. ul Haq, Structural, dielectric and electrical properties of Gd-substituted lithium nano-ferrites prepared by the WOWS sol–gel method, *Nanotechnology*, 31 (2020) 255707.
- [12] R. Zakir, S.S. Iqbal, A.U. Rehman, S. Nosheen, T.S. Ahmad, N. Ehsan, F. Inam, Spectral, electrical, and dielectric characterization of Ce-doped Co-Mg-Cd spinel nano-ferrites synthesized by the sol-gel auto combustion method, *Ceramics International*, 47 (2021) 28575-28583.
- [13] J. Rodney, S. Deepapriya, P. Annie Vinosha, M. Cyril Robinson, S. Krishnan, S. Martin Britto Dhas, S. Jerome Das, Impact of Synthesis Technique on Lanthanum Doped Copper Oxide Nanocrystals, an Alternative Counter Electrode for Pt-Free Dye-Sensitized Solar Cells, *Journal of nanoscience and nanotechnology*, 20 (2020) 4023-4034.
- [14] I. ALIa, N. Amin, A. REHMAN, M. Akhtar, M. Fatima, K. Mahmood, A. ALIa, G. Mustafa, M. Hasan, A. Bibi, Biostructures, ELECTRICAL AND MAGNETIC PROPERTIES OF BaCo<sub>x</sub>Cd<sub>2-x</sub>Fe<sub>16</sub>O<sub>27</sub> W-TYPE HEXAFERRITES (0 ≤ x ≤ 0.5), *Digest Journal of Nanomaterials & Biostructures*, 15 (2020).
- [15] N. Amin, M. Akhtar, M. Sabir, K. Mahmood, A. ALIa, G. Mustafa, M. Hasan, A. Bibi, M. Iqbal, F. Iqbal, SYNTHESIS, STRUCTURAL AND OPTICAL PROPERTIES OF Zn-SUBSTITUTED Co W-FERRITES BY COPRECIPITATION METHOD, *Journal of Ovonic Research*, 16 (2020) 11-19.
- [16] K. Hussain, N. Amin, M.I. Arshad, Evaluation of structural, optical, dielectric, electrical, and magnetic properties of Ce<sup>3+</sup> doped Cu<sub>0.5</sub>Cd<sub>0.25</sub>Co<sub>0.25</sub>Fe<sub>2-x</sub>O<sub>4</sub> spinel nano-ferrites, *Ceramics International*, 47 (2021) 3401-3410.

- [17] H.T. Ali, M. Ramzan, M.I. Arshad, N.A. Morley, M.H. Abbas, M. Yusuf, A.U. Rehman, K. Mahmood, A. Ali, N. Amin, Tailoring the optical, and magnetic properties of La-BaM hexaferrites by Ni substitution, *Chinese Physics B*, (2021). <https://doi.org/10.1088/1674-1056/ac1412>
- [18] M.N. Akhtar, A.B. Sulong, M. Akhtar, M.A. Khan, Systematic study of Ce<sup>3+</sup> on the structural and magnetic properties of Cu nanosized ferrites for potential applications, *Journal of Rare earths*, 36 (2018) 156-164.
- [19] K. Elayakumar, A. Dinesh, A. Manikandan, M. Palanivelu, G. Kavitha, S. Prakash, R.T. Kumar, S.K. Jaganathan, A. Baykal, Structural, morphological, enhanced magnetic properties and antibacterial bio-medical activity of rare earth element (REE) cerium (Ce<sup>3+</sup>) doped CoFe<sub>2</sub>O<sub>4</sub> nanoparticles, *Journal of Magnetism and Magnetic Materials*, 476 (2019) 157-165.
- [20] S. Bahhar, H. Lemziouka, A. Boutahar, H. Bioud, H. Lassri, E. Hlil, Influence of La<sup>3+</sup> site substitution on the structural, magnetic and magnetocaloric properties of ZnFe<sub>2-x</sub>La<sub>x</sub>O<sub>4</sub> (x = 0.00, 0.001, 0.005 and 0.01) spinel zinc ferrites, *Chemical Physics Letters*, 716 (2019) 186-191.
- [21] P. Kumar, S. Sharma, M. Knobel, M. Singh, Effect of La<sup>3+</sup> doping on the electric, dielectric and magnetic properties of cobalt ferrite processed by co-precipitation technique, *Journal of Alloys and Compounds*, 508 (2010) 115-118.
- [22] A. Aslam, A.U. Rehman, N. Amin, M.A. un Nabi, Q. ul ain Abdullah, N. Morley, M.I. Arshad, H.T. Ali, M. Yusuf, Z. Latif, Lanthanum doped Zn<sub>0.5</sub>Co<sub>0.5</sub>La<sub>x</sub>Fe<sub>2-x</sub>O<sub>4</sub> spinel ferrites synthesized via co-precipitation route to evaluate structural, vibrational, electrical, optical, dielectric, and thermoelectric properties, *Journal of Physics and Chemistry of Solids*, 154 (2021) 110080.
- [23] S. Qamar, M.N. Akhtar, K.M. Batoor, E. Raslan, Structural and magnetic features of Ce doped Co-Cu-Zn spinel nanoferrites prepared using sol gel self-ignition method, *Ceramics International*, 46 (2020) 14481-14487.
- [24] C. Murugesan, G. Chandrasekaran, Impact of Gd<sup>3+</sup> substitution on the structural, magnetic and electrical properties of cobalt ferrite nanoparticles, *RSC advances*, 5 (2015) 73714-73725.
- [25] M. Kamran, M. Anis-ur-Rehman, Enhanced transport properties in Ce doped cobalt ferrites nanoparticles for resistive RAM applications, *Journal of Alloys and Compounds*, 822 (2020) 153583.
- [26] A. Omelyanchik, K. Levada, S. Pshenichnikov, M. Abdolrahim, M. Baricic, A. Kapitunova, A. Galieva, S. Sukhikh, L. Astakhova, S. Antipov, Green Synthesis of Co-Zn Spinel Ferrite Nanoparticles: Magnetic and Intrinsic Antimicrobial Properties, *Materials*, 13 (2020) 5014.
- [27] P. Himakar, N. Murali, D. Parajuli, V. Veeraiah, K. Samatha, T.W. Mammo, M.B. Khalid, H. Muhammad, H.R. Emad, S.F. Adil, Magnetic and DC Electrical Properties of Cu Doped Co-Zn Nanoferrites, *Journal of Electronic Materials*, (2021) 1-9.
- [28] P. Thakur, R. Sharma, M. Kumar, S. Katyayal, N. Negi, N. Thakur, V. Sharma, P. Sharma, Superparamagnetic La doped Mn-Zn nano ferrites: dependence on dopant content and crystallite size, *Materials Research Express*, 3 (2016) 075001.
- [29] D. Mane, D. Birajdar, S. Patil, S.E. Shirsath, R. Kadam, Redistribution of cations and enhancement in magnetic properties of sol-gel synthesized Cu<sub>0.7-x</sub>Co<sub>x</sub>Zn<sub>0.3</sub>Fe<sub>2</sub>O<sub>4</sub> (0 ≤ x ≤ 0.5), *Journal of sol-gel science and technology*, 58 (2011) 70-79.
- [30] P. Dey, R. Das, Effect of silver doping on the elastic properties of CdS nanoparticles, *Indian Journal of Physics*, 92 (2018) 1099-1108.
- [31] R. Das, S. Sarkar, Determination of intrinsic strain in poly (vinylpyrrolidone)-capped silver nano-hexapod using X-ray diffraction technique, *Current Science*, (2015) 775-778.

- [32] D. Nath, F. Singh, R. Das, X-ray diffraction analysis by Williamson-Hall, Halder-Wagner and size-strain plot methods of CdSe nanoparticles-a comparative study, *Materials Chemistry and Physics*, 239 (2020) 122021.
- [33] F. Hamed, T. Ramachandran, V. Kurapati, The effect of induced strains on the optical band gaps in lanthanum-doped zinc ferrite nanocrystalline powders, *Modern Physics Letters B*, 30 (2016) 1650230.
- [34] A. Aslam, A. Razzaq, S. Naz, N. Amin, M.I. Arshad, M.A.U. Nabi, A. Nawaz, K. Mahmood, A. Bibi, F. Iqbal, N. Magnetism, Impact of Lanthanum-Doping on the Physical and Electrical Properties of Cobalt Ferrites, *Journal of Superconductivity and Novel Magnetism*, 1-10.
- [35] N. Amin, M.S.U. Hasan, Z. Majeed, Z. Latif, M.A. un Nabi, K. Mahmood, A. Ali, K. Mehmood, M. Fatima, M. Akhtar, Structural, electrical, optical and dielectric properties of yttrium substituted cadmium ferrites prepared by Co-Precipitation method, *Ceramics International*, 46 (2020) 20798-20809.
- [36] H. Anwar, A. Maqsood, Enhancement of electrical and magnetic properties of Cd<sup>2+</sup> doped Mn-Zn soft nanoferrites prepared by the sol-gel autocombustion method, *Journal of magnetism and magnetic materials*, 333 (2013) 46-52.
- [37] K.A. Ganure, L.A. Dhale, S.E. Shirsat, K.S. Lohar, Morphological study of lanthanum-doped nano spinel ferrite via normal micelles method, *Journal of Inorganic and Organometallic Polymers and Materials*, 28 (2018) 1821-1828.
- [38] V. Chaudhari, S.E. Shirsath, M. Mane, R. Kadam, S. Shelke, D. Mane, Crystallographic, magnetic and electrical properties of Ni<sub>0.5</sub>Cu<sub>0.25</sub>Zn<sub>0.25</sub>La<sub>x</sub>Fe<sub>2-x</sub>O<sub>4</sub> nanoparticles fabricated by sol-gel method, *Journal of Alloys and Compounds*, 549 (2013) 213-220.
- [39] A. Aslam, N. Morley, N. Amin, M.I. Arshad, M.A. un Nabi, A. Ali, K. Mahmood, A. Bibi, F. Iqbal, S. Hussain, Study of structural, optical and electrical properties of La<sup>3+</sup> doped Mg<sub>0.25</sub>Ni<sub>0.15</sub>Cu<sub>0.25</sub>Co<sub>0.35</sub>Fe<sub>2-x</sub>La<sub>x</sub>O<sub>4</sub> spinel ferrites, *Physica B: Condensed Matter*, 602 (2021) 412565.
- [40] R. Kershi, Rare-earth ions as a key influencer on the magnetic, spectroscopic and elastic properties of Er<sub>γ</sub>Zn<sub>0.2</sub>Co<sub>0.8</sub>Fe<sub>2-γ</sub>O<sub>4</sub> nanoparticles, *Journal of Alloys and Compounds*, 864 (2021) 158114.
- [41] R.Kershi, Spectroscopic, elastic, magnetic and optical studies of nanocrystallite and nanoferro-fluids Co ferrites towards optoelectronic applications, *Materials Chemistry and Physics*, 248 (2020) 122941.
- [42] M.Z. Shoushtari, A. Emami, S. Ghahfarokhi, A study of the doped zinc-ferrite nanoparticles with bismuth, *Materials Research Express*, 5 (2018) 075024.
- [43] I. Gul, A. Maqsood, Structural, magnetic and electrical properties of cobalt ferrites prepared by the sol-gel route, *Journal of Alloys and Compounds*, 465 (2008) 227-231.
- [44] K. Hussain, A. Bibi, F. Jabeen, N. Amin, K. Mahmood, A. Ali, M.Z. Iqbal, M.I. Arshad, Study of structural, optical, electrical and magnetic properties of Cu<sup>2+</sup> doped Zn<sub>0.4</sub>Co<sub>0.6x</sub>Ce<sub>0.1</sub>Fe<sub>1.9</sub>O<sub>4</sub> spinel ferrites, *Physica B: Condensed Matter*, 584 (2020) 412078.
- [45] W. Mohamed, M. Alzaid, M. SM Abdelbaky, Z. Amghouz, S. García-Granda, A. Abu-Dief, Impact of Co<sup>2+</sup> substitution on microstructure and magnetic properties of Co<sub>x</sub>Zn<sub>1-x</sub>Fe<sub>2</sub>O<sub>4</sub> nanoparticles, *Nanomaterials*, 9 (2019) 1602.
- [46] M.N. Akhtar, M.S. Nazir, Z. Tahir, S. Qamar, M. Khan, Impact of Co doping on physical, structural, microstructural and magnetic features of MgZn nanoferrites for high frequency applications, *Ceramics International*, 46 (2020) 1750-1759.
- [47] A. Majeed, M.A. Khan, F. ur Raheem, A. Hussain, F. Iqbal, G. Murtaza, M.N. Akhtar, I. Shakir, M.F. Warsi, M. Materials, Structural elucidation and magnetic behavior evaluation of rare earth (La, Nd, Gd, Tb, Dy) doped BaCoNi-X hexagonal nano-sized ferrites, *Journal of Magnetism and Magnetic Materials*, 408 (2016) 147-151.

- [48] S. Gaba, A. Kumar, P.S. Rana, M. Arora, Influence of  $\text{La}^{3+}$  ion doping on physical properties of magnesium nanoferrites for microwave absorption application, *Journal of Magnetism and Magnetic Materials*, 460 (2018) 69-77.
- [49] I.P. Muthuselvam, R. Bhowmik, Structural phase stability and magnetism in  $\text{Co}_2\text{FeO}_4$  spinel oxide, *Solid State Sciences*, 11 (2009) 719-725.
- [50] W. Zhang, A. Sun, X. Zhao, N. Suo, L. Yu, Z. Zuo, Structural and magnetic properties of  $\text{La}^{3+}$  ion doped Ni–Cu–Co nano ferrites prepared by sol–gel auto-combustion method, *Journal of Sol-Gel Science and Technology*, 90 (2019) 599-610.
- [51] I.P. Muthuselvam, R. Bhowmik, Mechanical alloyed  $\text{Ho}^{3+}$  doping in  $\text{CoFe}_2\text{O}_4$  spinel ferrite and understanding of magnetic nanodomains, *Journal of Magnetism and Magnetic Materials*, 322 (2010) 767-776.